

An advanced spatial co-registration of cloud properties for the atmospheric Sentinel missions: Application to TROPOMI

Athina Argyrouli^{1,2}, Diego Loyola², Fabian Romahn², Ronny Lutz², Víctor Molina García², Pascal Hedelt², Klaus-Peter Heue², and Richard Siddans³

¹Technical University of Munich (TUM), Chair of Remote Sensing Technology, School of Engineering and Design, Munich, Germany

²German Aerospace Center (DLR), Remote Sensing Technology Institute (IMF), Wessling, Germany

³Rutherford Appleton Laboratory (RAL), Chilton OX11 0QX, United Kingdom

Correspondence: Ronny Lutz (Ronny.Lutz@dlr.de)

Abstract. The retrieval of cloud parameters from the atmospheric Sentinel missions require Earth reflectance measurements from a set of spectral bands. [The ground pixels of the involved spectral bands should be fully aligned but when they are not, a special treatment is required within the operational algorithms.](#) This so-called inter-band spatial mis-registration of passive spectrometers is present when the Earth reflectance measurements in different spectral bands are captured by different spectrometers. The cloud retrieval algorithm requires reflectance measurements in the UV (ultraviolet)/VIS (visible) band, where the first cloud parameter (i.e., radiometric cloud fraction) is retrieved from the OCRA (Optical Cloud Recognition Algorithm) algorithm. In addition, Earth reflectances in the NIR (near-infrared) band are needed for the retrieval of two additional cloud parameters (i.e., cloud height and cloud albedo or cloud-top height and optical thickness) from the ROCINN (Retrieval of Cloud Information using Neural Networks) algorithm. In the former TROPOMI (TROPOspheric Monitoring Instrument)/S5P (Sentinel-5 Precursor) retrieval, a co-registration scheme of the derived cloud parameters from the source band to the target band based on pre-calculated mapping weights from UV/VIS to NIR, and vice versa, is applied. In this paper we present a new scheme for the co-registration of the TROPOMI cloud parameters using collocated VIIRS (Visible Infrared Imaging Radiometer Suite)/SNPP (Suomi National Polar-orbiting Partnership) information. [The new co-registration scheme based on the VIIRS data improves the TROPOMI cloud product quality and allows the addition of cloud information for the first \(westernmost\) TROPOMI UVIS ground pixel. The latter practically means that a significant number of valid data points are included to the TROPOMI cloud, total ozone, SO₂ and HCHO product since November 26th 2023 \(orbit 31705\), when the new co-registration scheme became operational.](#) From a comparison analysis between the two techniques, we found that the largest differences mainly appear for inhomogeneous scenes. From a validation exercise of TROPOMI against VIIRS in the across-track flight direction, we found that the old co-registration scheme tends to smooth out cloud structures along the scanline, whereas such structures can be maintained with the new scheme. The need to implement a similar inter-band spatial co-registration scheme is foreseen for the Sentinel-4/MTG-S (Meteosat Third Generation - Sounder) and Sentinel-5/MetOp-SG (Meteorological Operational Satellite - Second Generation) missions. In the case of Sentinel-4 instrument, the external cloud information will originate from collocated FCI (Flexible Combined Imager) data, on board the MTG-I (Meteosat Third Generation - Imager) satellite.

Table 1. Spectral information for the TROPOMI spectrometers: The reflectance measurements are organized according to the 8 spectral bands BD1-BD8 covered by the 4 spectrometers UV, UVIS, NIR and SWIR.

Spectrometer	UV		UVIS		NIR		SWIR	
Wavelength range [nm]	267-300	300-332	305-400	400-499	661-725	725-786	2300-2343	2343-2389
Band ID	BD1	BD2	BD3	BD4	BD5	BD6	BD7	BD8

25 *Copyright statement.* TEXT

1 Introduction

The operational algorithms for the retrieval of cloud parameters from the atmospheric Sentinel missions make use of Earth-shine reflectance measurements in the spectral windows of UV, VIS and NIR. Often those reflectances are captured from different spectrometers. For instance, the TROPOMI payload on board Sentinel-5 Precursor covers four distinct spectrometers (see Table 1) and each spectrometer of them is split electronically in two bands (i.e., UV-1 and 2, UVIS-1 and 2, NIR-1 and 2, and shortwave infrared (SWIR) 1 and 2), see Veefkind et al. (2012). Using different spectrometers leads to different ground pixels for the several bands that are not perfectly aligned, which is called inter-band spatial mis-registration. Although it is much smaller than between different spectrometers, mis-alignment between ground pixels could also occur within the same spectrometer (Kleipool et al., 2018). The ground pixel mis-alignment is inter-connected to the across-flight spatial resolution of UVIS/NIR TROPOMI measurements, which is equal to 3.5 km² in the center of the swath and in a large area around it.

The TROPOMI operational cloud algorithms OCRA/ROCINN (Loyola et al., 2018) have a long-standing heritage and have already been applied operationally to a large number of instruments starting with GOME (Global Ozone Monitoring Experiment) on ERS-2 (European Remote Sensing Satellite) (Loyola et al., 2010). OCRA/ROCINN, described in Section 2, has been adapted for several follow-up missions including SCIAMACHY (SCanning Imaging Absorption spectromETER for Atmospheric CartographY) on ENVISAT (ENViromental SATellite) (Loyola, 2004), the GOME-2 instruments on board MetOp-A/B/C (Meteorological Operational satellite) (Lutz et al., 2016), and the EPIC (Earth Polychromatic Imaging Camera) instrument on the DSCOVR (Deep Space Climate Observatory) satellite, located at the Lagrangian point L1 (Molina García, 2022). Furthermore, OCRA/ROCINN will be applied operationally to the Sentinel-4 instrument.

2 The operational cloud algorithm

45 The operational processing of cloud products under DLR responsibility is performed using the UPAS (Universal Processor for Atmospheric Spectrometers) system. The two-step algorithm used for the UPAS cloud processing makes possible the

simultaneous retrieval of three cloud properties as described in (Loyola et al., 2018). The first step is to derive the radiometric cloud fraction f_c in the UV/VIS spectral region. The OCRA algorithm retrieves the cloud fraction from the total measured reflectance by considering that the measured reflectance contains two contributions; one from the cloud-free background and a second one from the clouds. OCRA requires the clear-sky reflectance maps obtained from the same instrument (Lutz et al., 2016). The main assumption of the OCRA algorithm is a wavelength independency of the cloudy spectrum reflectance over the considered wavelength ranges. This means that the reflectance for a fully cloudy pixel is equal for all considered OCRA colors, resulting in a "white" scene when the reflectances are transferred to color space. The second step is to retrieve two additional cloud parameters within the O₂ A-band window (Schuessler et al., 2014) using the ROCINN algorithm. By using the independent pixel approximation (IPA) concept (Cahalan et al., 1994; Chambers et al., 1997), the sun-normalized radiances can be expressed as the summation of two components for the cloud-free and cloudy part of the pixel using the retrieved OCRA cloud fraction (see Equations 1 and 2). Several atmospheric conditions, with and without clouds, are simulated using LIDORT (Linearized Discrete Ordinate Radiative Transfer radiances) (Spurr, 2006). For the cloudy skies, the simulations are performed for two different cloud models. The Cloud-as-Reflecting-Boundaries (CRB) model is a simplistic approach which assumes that the cloud performs as a Lambertian reflector. The retrieved cloud parameters from the CRB model are the cloud albedo A_c and the cloud height Z_c . Provided that this model contains a cloud which behaves like a simple reflecting boundary and does not have any geometrical extend, the retrieved height should not be considered as the height of the cloud top but the height at the radiometric middle of the cloud. A more sophisticated approach, called Cloud-As-Layer (CAL) parameterizes the cloud as a layer of liquid water particles with their scattering properties derived from the Mie theory (Van de Hulst, 1957; Bohren and Huffman, 1983). In this model, the cloud has a predefined geometrical thickness. The retrieved quantities are the cloud-top height Z_{ct} and the cloud optical thickness τ_c . The following mathematical expressions refer to the simulated CRB and CAL sun-normalized radiances with R_s being the radiance from the ground and R_c the radiance from the cloud at the wavelength λ :

$$R_{sim}^{CRB}(\lambda) = (1 - f_c) R_s(\lambda, \theta, A_s, Z_s) + f_c R_c(\lambda, \theta, A_c, Z_c) \quad (1)$$

$$R_{sim}^{CAL}(\lambda) = (1 - f_c) R_s(\lambda, \theta, A_s, Z_s) + f_c R_c(\lambda, \theta, \tau_c, Z_{ct}, Z_{cb}, A_s, Z_s) \quad (2)$$

where Z_s is the surface height, A_s the surface albedo, θ the path geometry and Z_{cb} the cloud bottom height, which is fixed at 1 km below the cloud-top height. Table 2 summarizes the retrieved parameters from the operational cloud algorithm with the usual abbreviation notation and the corresponding mathematical symbol.

The cloud fraction, estimated by OCRA using image analysis, is a radiometric cloud fraction and does not necessarily match in all situations with a geometric cloud fraction as defined in the standard IPA. Since OCRA determines the cloud fraction based on how much the TOA reflectances differ from the expected TOA reflectances under clear-sky conditions, it is not possible under all circumstances to discriminate if the TOA reflectance discrepancy is caused by a fully-cloudy scene with small COT or a partially-cloudy scene with high COT. For limit cases with low COT (≤ 5), it can be observed that the OCRA radiometric

Table 2. List of cloud parameters, abbreviations and mathematical symbols referring to the operational cloud algorithm.

Parameter (Abbreviation)	Retrieval Algorithm	Symbol
Cloud Fraction (CF)	OCRA	f_c
Cloud Height (CH)	ROCINN_CRB	Z_c
Cloud-Top Height (CTH)	ROCINN_CAL	Z_{ct}
Cloud Albedo (CA)	ROCINN_CRB	A_c
Cloud Optical Thickness (COT)	ROCINN_CAL	τ_c

cloud fraction tends to be much lower than the geometric cloud fraction, and this discrepancy tends to be compensated in ROCINN by retrieving a higher COT value.

80 In the UPAS environment, LIDORT simulations are parameterized using Neural Networks (NNs) in order to speed up the forward model simulations and be able to process in near-real-time (NRT) the large data volume of TROPOMI. For each input parameter (like Z_{ct} , τ_c etc.), a range is predefined and a large number of samples is generated using the smart sampling technique (Loyola et al., 2016). Then, the training set for the NN is generated by computing simulated radiances for all the sampling sets. This part is the most computationally expensive as it requires line-by-line LIDORT calculations but it is only
85 done once and offline. The accuracy of the NN is assessed by comparing the forward model simulations with samples not used in the NN training.

3 Special treatment of the mis-registration within the OCRA/ROCINN algorithm tandem: application on existing mission

The OCRA/ROCINN algorithm is the operational algorithm for the TROPOMI L2 cloud product within the Sentinel-5 Precursor mission. This section describes the old co-registration approach and introduces the new approach which is implemented in addition to the old co-registration scheme for the operational S5P cloud algorithm. The mis-alignment of TROPOMI ground pixels from the UVIS and NIR spectrometers is illustrated in Fig. 1. The ground pixels of the detector rows 15-25 are shown for 5 continuous scanlines. Each TROPOMI scanline contains 450 pixels in BD3 and 448 pixels in BD6. In general, the BD6 ground pixels appear shifted towards the East w.r.t. the BD3 ground pixels. The spatial mis-alignment in the across-track direction is not a fixed number but instead it depends on the position in the swath since the ground pixels at nadir are different
95 in size than at the swath edges. The ground pixel size is 3.5 km in the center of the swath and in a large area around it, but it becomes larger towards the edges of the swath due to the Earth's curvature and the instrument large swath angle. The so-called binning factors are selected to optimize the signal-to-noise ratio per pixel with the aim to minimize the difference in ground pixel size in the across-track direction. For the TROPOMI radiance measurements in BD3, BD4 and BD6, which are inputs

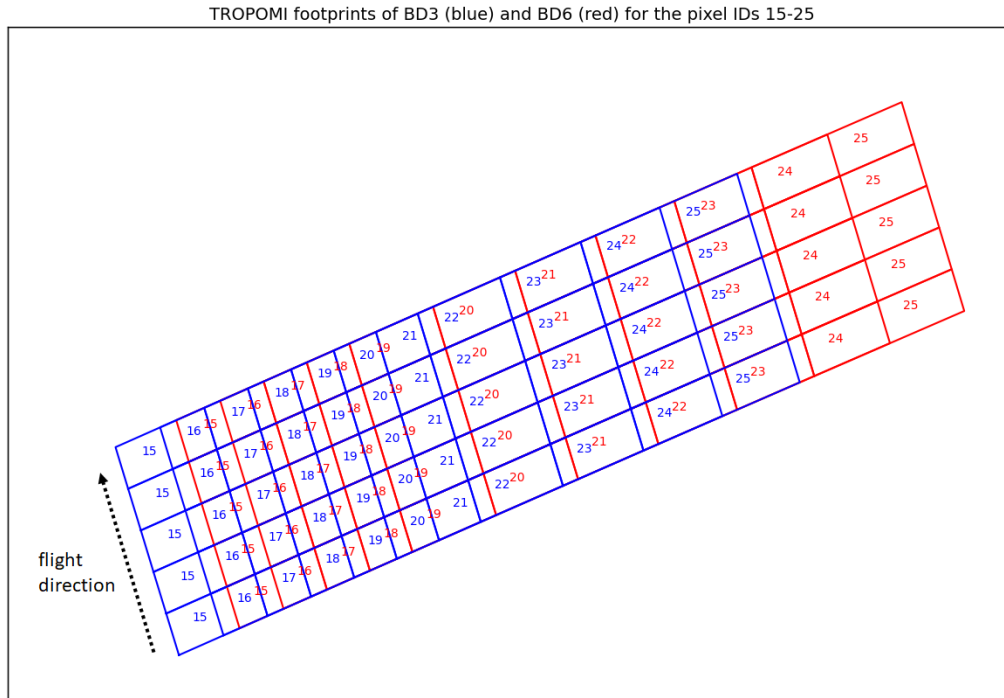


Figure 1. TROPOMI ground pixels for the VIS-1 and NIR-2 spectrometers. The Band IDs for TROPOMI are described in Table 1: BD3 (with blue) refers to VIS-1 spectrometer and BD6 (with red) refers to NIR-2 spectrometer.

100 to OCRA/ROCINN, a binning factor of 2 is used in the center and in a large region around it resulting to the ground pixel size of 3.5 km. At the edges of the swath the binning factor is reduced from 2 to 1 in order to keep the ground pixel size at a reasonable value. Due to optical limitations of the instrument and the curvature of the Earth, the ground pixel size at the edges of the swath is about 15 km (KNMI, 2022). The smallest mis-placement in the across-track direction is found at the center of the swath and it is about half a detector pixel, which is translated to about 1.75 km at nadir. Higher mis-alignment between

105 BD3 and BD6 ground pixels, which can reach up to about 4 km, is present at the east edge of the swath. The co-registration needs to be performed in the across-track direction since there is no mis-match in the in-flight direction. The complementary instrument, which is used for the treatment of the spatial mis-registration of TROPOMI, is VIIRS on board the Suomi National Polar-orbiting Partnership. S5P satellite is located at a low Earth orbit (LEO) and crosses the equator in an ascending node at 13.30 h mean local solar time. This facilitates the so-called loose formation operation with the SNPP spacecraft, with only

110 3 to 5 minutes time difference from S5P. The spatial resolution of VIIRS at nadir is 750 m. The VIIRS cloud products are

re-gridded to the TROPOMI ground pixels as part of the S5P-NPP Cloud processor (Siddans, 2016). The pioneer methodology to improve the existing co-registration scheme from the UV/VIS to NIR and the NIR to UV/VIS using collocated imager data is presented in Sect. 3.3.1 and 3.3.2, respectively.

3.1 Previous treatment of the spatial mis-registration in the operational UPAS system

115 Due to the spatial mis-registration between the [TROPOMI BD3](#) and BD6 bands, the operational cloud product contains a flag called Cloud Co-registration Inhomogeneity Flag (CCIF). This flag is raised after the Cloud Co-registration Inhomogeneity Parameter (CCIP), which is defined as the weighted averaged gradient of cloud fractions

$$\text{CCIP}_j = \frac{\sum_i w_{ij} |f_{ci} - f_{cj}|}{\sum_i w_{ij}}, \quad (3)$$

where the weights w_{ij} correspond to the co-registration mapping values between UVIS bands (source, index i) and the NIR
120 band (target, index j). [The \$w_{ij}\$ weights and the \$f_{cj}\$ cloud fraction in the NIR grid are estimated with the use of the mapping tables from \(Sneep, 2015\) as described below.](#) The CCIF is raised if the CCIP is larger than 0.4. The aforementioned threshold has been selected based on tests from VIIRS cloud product re-sampled to the TROPOMI spatial grid.

Since UPAS version 2.0, the co-registration method is based on pre-calculated mapping weights (Sneep, 2015) between
125 BD3 and BD6 as illustrated in Fig. 2. This method for combining information from different bands is based on the fractions of overlapping areas between the source and target pixels. The weights sum up to a total 1.0 and the most common situation is that two source pixels contribute to the target pixel with very few exceptions, which are discussed later in the following Sect. 3.3.1 and 3.3.2. When the co-registration is done from BD3 to BD6, the BD6 target pixels have a difference of 1, 2 or 3 pixels towards the East direction. When the co-registration is done from BD6 to BD3, the BD3 target pixels have a difference of 1, 2 or 3 pixels towards the West direction.

130 3.2 Evaluation of OCRA/ROCINN cloud properties for the TROPOMI instrument

Recent validation studies of the TROPOMI cloud properties against other satellite sensors (i.e., VIIRS, OMI (Ozone Monitoring Instrument), MODIS (Moderate Resolution Imaging Spectroradiometer)) and the ground-based CloudNet network discussed the similarities and differences between VIIRS and TROPOMI cloud parameters (Compernelle et al., 2021). The VIIRS geometrical cloud fraction is usually higher than the OCRA radiometric cloud fraction because of the different definition but there
135 is an analogy between the two cloud fractions. One exception for the positive differences between VIIRS and OCRA cloud fraction is the sun-glint region, where the dark ocean is perceived as a bright surface and very often misinterpreted as clouds. The magnitude of the sun-glint effect and the affected area depends on the smoothness of the ocean, which is determined by the wind properties over the ocean surface (Cox and Munk, 1954). The operational S5P cloud products include a flag indicating the occurrence of sunglint. Similarly, the cloud height derived from TROPOMI is usually below the cloud-top height from VIIRS
140 because the infra-red bands of VIIRS are more sensitive to clouds than the UVN bands from TROPOMI.

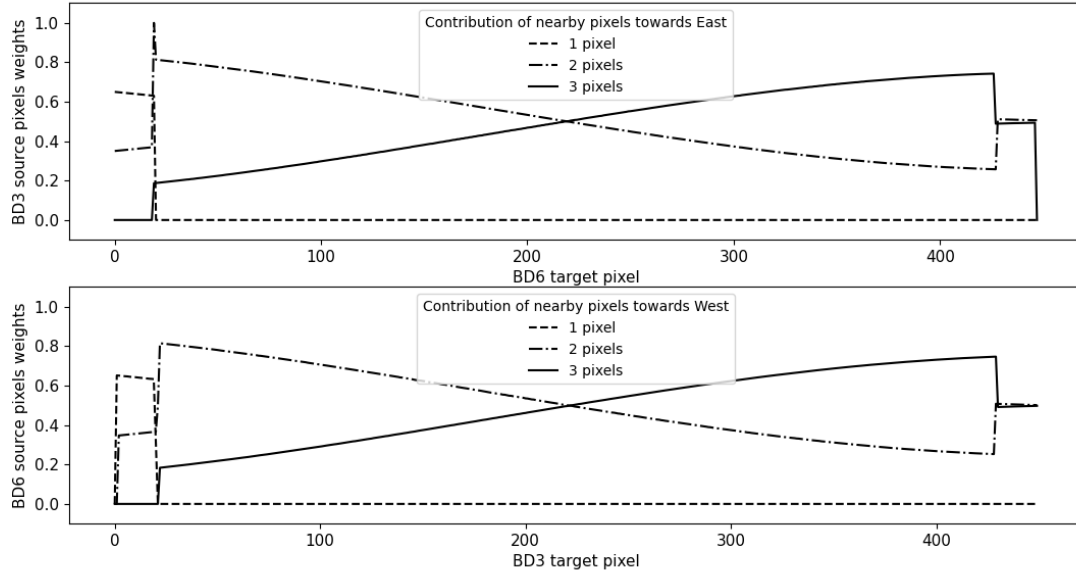


Figure 2. Weights from the static mapping tables (Sneep, 2015) used in the old co-registration scheme for Sentinel-5P. The upper panel refers to the mapping from UVIS source band to NIR target band. The lower panel refers to the mapping from NIR source band to UVIS target band.

The need to handle the spatial mis-registration between TROPOMI UVIS and NIR bands with a more dynamic and advanced approach was highlighted after the evaluation of OCRA/ROCINN cloud properties for the TROPOMI instrument. Recent inter-comparison studies between TROPOMI cloud products, with the focus on cloud properties needed for trace gas retrievals, showed that the co-registration has an impact along the cloud edges (Latsch et al., 2022). The proper co-registration of the cloud properties is not only required for the improvement of the operational TROPOMI cloud product itself, but for the direct impact that clouds have on the accurate retrieval of trace gases including total ozone (Spurr et al., 2021), tropospheric ozone (Heue et al., 2018), HCHO (De Smedt et al., 2018) and SO₂ (Theys et al., 2017).

3.3 Advancement in the co-registration approach with the synergistic use of VIIRS cloud data

VIIRS has a much finer spatial resolution than TROPOMI, which is 750 m at nadir. With this high spatial resolution, VIIRS captures small-scale cloud structures. VIIRS collects measurements in several spectral windows: VIS/NIR band, mid-IR and LW IR, which makes its cloud product more sensitive to optically thin ice clouds.

The VIIRS cloud products are re-gridded to the TROPOMI ground pixels as part of the S5P-NPP Cloud processor (Siddans, 2016). An auxiliary product, which contains cloud information relevant to each TROPOMI ground pixel, can be derived from observations captured by the VIIRS instrument. This operational L2 auxiliary product is called S5P-NPP Cloud product and

155 developed by the Rutherford Appleton Laboratory (Siddans, 2022). In this work, we present how the S5P-NPP cloud data is
 used for the co-registration of the cloud product from BD3 to BD6 and vice versa. The S5P-NPP cloud product accepts as
 inputs a set of cloud-related VIIRS EDRs (Environmental Data Records): (a) the CloudMask which is necessary for the co-
 registration of OCRA cloud fraction, (b) the CloudHeight EDR mandatory for the co-registration of ROCINN cloud height and
 (c) the CloudDCOMP (Daytime Cloud Optical and Microphysical Properties) EDR for the co-registration of ROCINN cloud
 160 albedo/optical thickness.

The VIIRS Enterprise Cloud Mask (ECM) describes the area of the earth's horizontal surface that is masked by the vertical
 projection of detectable clouds (Heidinger and Straka, 2020). The ECM combines spectral and spatial tests to produce a 4-
 level classification of cloudiness of the ECM cloud mask $\delta_{jk}^{CM=X}$, where X is any of the following categories: confidently clear,
 probably clear, probably cloudy, confidently cloudy. Apart from solar reflectances in the VIS, the ECM makes use of spectral
 165 channels in the IR that are more sensitive to clouds. The retrieval method is based on a naive Bayesian approach as part of a
 library of machine learning (ML) methods, already [successfully](#) applied within Pathfinder Atmospheres Extended (PATMOS-x)
 (Heidinger et al., 2012).

For the co-registration of TROPOMI cloud fraction, an equivalent VIIRS cloud fraction M_c can be calculated as the number
 of confidently cloudy pixels divided by the sum of all four cloudiness classes:

$$170 \quad M_c = \frac{\delta_{jk}^{\text{ConfidentlyCloudy}}}{\delta_{jk}^{\text{ConfidentlyCloudy}} + \delta_{jk}^{\text{ProbablyCloudy}} + \delta_{jk}^{\text{ConfidentlyClear}} + \delta_{jk}^{\text{ProbablyClear}}} \cdot \quad (4)$$

The expression of the VIIRS cloud fraction M_c has been also calculated by considering the sum of confidently and prob-
 ably cloudy classes at the nominator. The difference was minor compared to the definition of Eq. 4 and therefore, the latter
[mathematical expression was considered most appropriate.](#)

VIIRS cloud-top height is defined for each cloud-covered Earth location as the set of heights above mean sea level of the
 175 tops of the cloud layers overlying the location (Heidinger et al., 2020). The Cloud Height Algorithm (ACHA) has already been
 applied for the retrieval of the cloud height property from several sensors like MODIS and GOES-16/17 (US Geostationary
 Operational Environmental Satellite R-series) ABI (Advanced Baseline Imager). ACHA makes use of only infrared channels
 in order to provide consistent products for both day and night time as well as the terminator conditions. It uses an analytical
 radiative transfer model embedded into an optimal estimation retrieval approach (Rodgers, 2000). The primary retrieved cloud
 180 property is the cloud-top temperature and, at a later step, the cloud-top pressure and cloud-top height are derived from the
 atmospheric temperature profile based on the Numerical Weather Prediction (NWP) data. For the co-registration of ROCINN
 CRB cloud height and ROCINN CAL cloud-top height, the cloud-top height variable in the EDR CloudHeight can be directly
 used. [VIIRS cloud-top height is denoted as \$H_c^{UV}\$ in the UVIS ground pixel and \$H_c^{NIR}\$ in the NIR ground pixel, respectively.](#)

VIIRS cloud optical thickness is defined as the optical thickness of the atmosphere due to cloud droplets, per unit cross
 185 section, integrated over every distinguishable cloud layer and all distinguishable cloud layers in aggregate, in a vertical column
 above a horizontal cell on the Earth's surface (Walther and Straka, 2020). The COT together with the Effective Particle Size
 and Liquid/Ice Water Path are the cloud properties retrieved from the Daytime Cloud and Optical and Microphysical Properties

(DCOMP) algorithm (Walther and Heidinger, 2012). The DCOMP algorithm works not only for VIIRS but for more sensors with observations in VIS and NIR. So far, it has been applied to the geo-stationary satellites SEVIRI (Spinning Enhanced Visible and InfraRed Imager), GOES R-series, MTSAT (Multifunctional Transport Satellites) and HIMAWARI and the polar-orbiting satellites NOAA-AVHRR (Advanced Very High Resolution Radiometer) series and MODIS. The retrieval approach is based on solving the radiative transfer equation for a single-layered, plane-parallel homogeneously distributed cloud. The retrieval originates from earlier methods that also retrieve cloud optical depth and cloud effective radius from visible and near-infrared wavelengths (King, 1987; Nakajima and King, 1990a, b).

For the co-registration of ROCINN CAL cloud optical thickness, the COT variable in the EDR CloudDCOMP can be directly used. For the co-registration of the cloud albedo, the following approximation conversion formula is used to bring the VIIRS cloud optical thickness (τ_c) to an equivalent cloud albedo (A_c) (Loyola, 2013; Kokhanovsky and Mayer, 2003):

$$A_c = 1 - \frac{1}{1.072 + 0.75\tau_c(1 - f_g)} \quad (5)$$

with f_g being the constant for water clouds equal to 0.85 and the other constant numbers derived from semi-empirical formulas (Kokhanovsky and Mayer, 2003). Similar conversion is required for the re-gridding of VIIRS cloud optical thickness to the TROPOMI ground pixels within the S5P-NPP Cloud processor, but there the cloud optical thickness is converted to an effective transmission (see Eq. 29 in Siddans (2016)).

3.3.1 New scheme for the co-registration of OCRA cloud fraction from UV/VIS to NIR

OCRA uses the reflectances from the UV/VIS spectral region and the co-registration is therefore done from the UV/VIS source band to the NIR target band. We denote with index j the row in the NIR grid and with index i the row in UV/VIS grid.

The most common situation is that two UV/VIS source pixels contribute to the NIR target pixel as demonstrated in Case A of Fig. 3. When those UV/VIS pixels from the imager have different cloud fraction values, the weight (γ) for the j^{th} target pixel is calculated according to the following mathematical formulation:

$$\gamma[j] = \frac{M_c^{\text{NIR}}[j] - M_c^{\text{UV}}[i+1]}{M_c^{\text{UV}}[i] - M_c^{\text{UV}}[i+1]}, \quad (6)$$

with the cloud fraction M_c derived from Equation 4. Then, the cloud fraction at the j^{th} target pixel is computed as:

$$f_c^{\text{NIR}}[j] = \gamma[j]f_c^{\text{UV}}[i] + (1 - \gamma[j])f_c^{\text{UV}}[i+1] \quad (7)$$

In case the neighboring UV/VIS pixels from the imager have equal cloud fraction values, the weight calculation is simplified as:

$$\gamma[j] = \frac{M_c^{\text{NIR}}[j]}{M_c^{\text{UV}}[i]}. \quad (8)$$

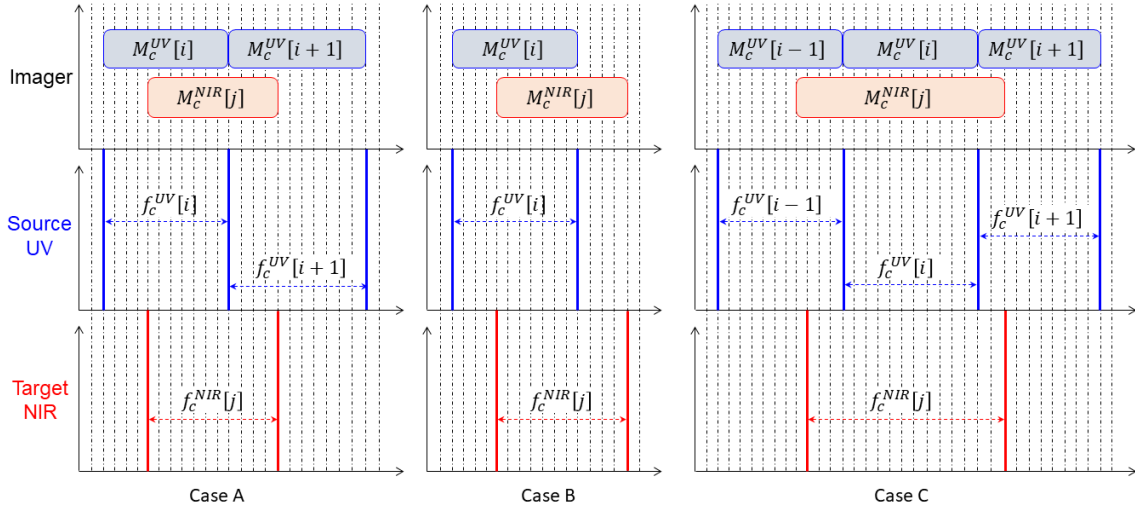


Figure 3. Co-registration of OCRA Cloud Fraction from UV/VIS to NIR: The UV/VIS ground pixels are denoted with the blue boxes and the NIR ground pixels with the red boxes. The dashed vertical lines compose a grid for illustration purposes. Case A (left diagram) shows the typical situation of 2 source pixels contributing to the target pixel, (b) Case B (middle diagram) shows the exception of 1 source pixel contributing to the target pixel and (c) Case C (right diagram) shows the exception of 3 source pixels contributing to the target pixel.

215 Special treatments need to be considered for cases with only partial overlap between source and target band. For example, in TROPOMI there is only partial overlap between the source and target band at the east part of the swath, as shown in Fig. 4. Therefore, the last target pixel of every scanline has the contribution of a single source pixel as illustrated in Case B of Fig. 3. The weight calculation for this pixel is done similarly to Equation 8, and the co-registered cloud fraction is then expressed as:

$$f_c^{NIR}[j] = \gamma[j] f_c^{UV}[i]. \quad (9)$$

220 Other exceptions might refer to pixels affected by a binning change, where the binning factor changes from 2 to 1 (see Sect. 3). For TROPOMI, the binning change at the East edge of the swath, which occurs at the target pixel number 19 of every scanline, creates a special case of three BD3 pixels contributing to the target BD6 pixel. Case C diagram of Fig.3 demonstrates this special situation where the calculation of two weighting factors is required; one between the $(i-1)^{th}$ and i^{th} pixel defined as γ_1 and a second one between the i^{th} and $(i+1)^{th}$ pixel defined as γ_2 .

$$225 \quad \gamma_1[j] = \frac{M_c^{NIR}[j] - M_c^{UV}[i]}{M_c^{UV}[i-1] - M_c^{UV}[i]} \quad (10)$$

$$\gamma_2[j] = \frac{M_c^{NIR}[j] - M_c^{UV}[i+1]}{M_c^{UV}[i] - M_c^{UV}[i+1]} \quad (11)$$

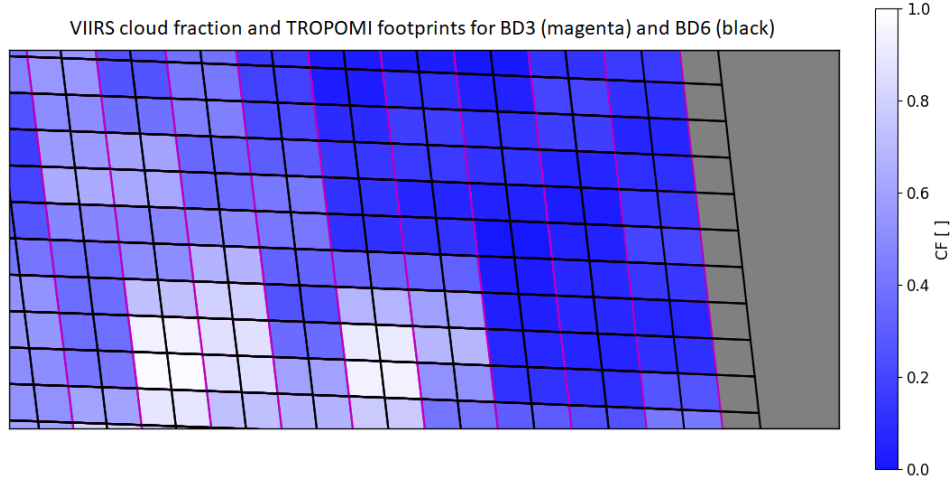


Figure 4. TROPOMI ground pixels for Bands 3 and 6 at the east edge of the orbit. Provided that the mis-match is only in the across-track direction, the horizontal magenta lines of BD3 overlap with the horizontal black lines of BD6.

with the final co-registered cloud fraction at the target NIR pixel expressed as following:

$$f_c^{\text{NIR}} [j] = \frac{1}{2} [\gamma_1 [j] f_c^{\text{UV}} [i-1] + (1 - \gamma_1 [j]) f_c^{\text{UV}} [i]] + \frac{1}{2} [\gamma_2 [j] f_c^{\text{UV}} [i] + (1 - \gamma_2 [j]) f_c^{\text{UV}} [i+1]]. \quad (12)$$

The binning factor change at the West edge of the swath does not create any exceptions (see Fig. 2) but falls into the typical Case A of two BD3 source pixels contributing to the BD6 target pixel.

Notice that the cloud fraction co-registration using VIIRS input is applicable to cloud scenes where M_c^{UV} contains different values in the adjacent contributing pixels, as the weight computation from Equation 6 is numerically impossible in scenes where $M_c^{\text{UV}} [i] = M_c^{\text{UV}} [i+1]$. This precludes the applicability of the new approach to VIIRS fully cloudy scenes. Due to this limitation, the calculation of independent weighting factors for each cloud parameter, based on different VIIRS input, is required. The co-registration of the ROCINN cloud height becomes possible also under fully cloudy scenes if the respective γ -factor is computed from VIIRS cloud top height H_c^{NIR} inputs.

3.3.2 New scheme for the co-registration of ROCINN cloud parameters from NIR to UV/VIS

ROCINN retrieves the additional cloud parameters in the Oxygen A-band of NIR (source band with index j). However, the trace gases are derived in a different band and need the cloud information in UV/VIS (target band with index i). When the co-registration takes place from NIR to UV/VIS, the most frequent scenario is that two source pixels contribute to the target pixel as shown in Case A of Fig. 5. Following Equation 6, the weight for the i^{th} UV/VIS target pixel is then calculated as:

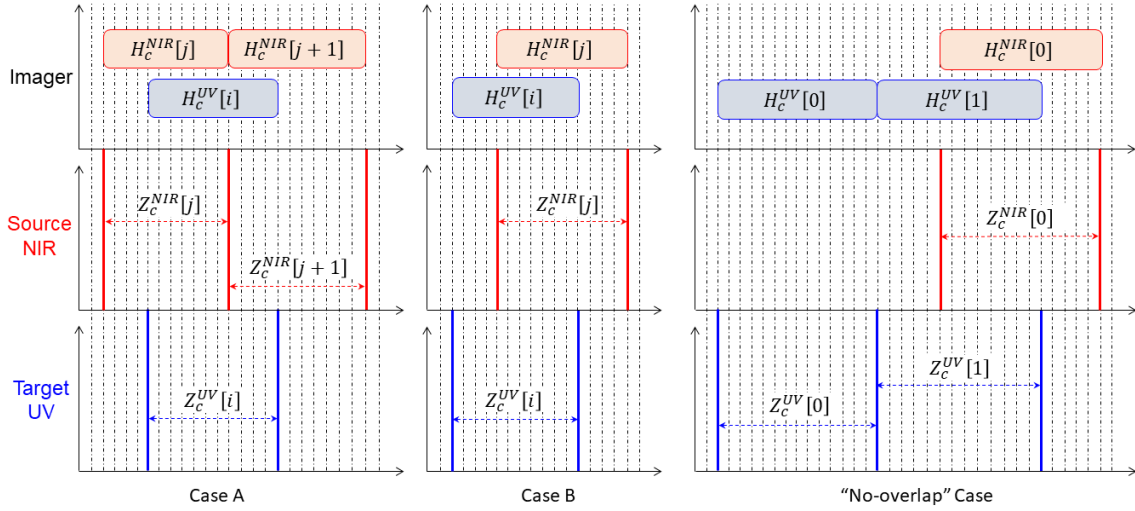


Figure 5. Co-registration of ROCINN Cloud Height from NIR to UV/VIS: The NIR ground pixels with the red boxes and the UV/VIS ground pixels are denoted with the blue boxes. The dashed vertical lines compose a grid for illustration purposes. Case A (left diagram) shows the typical situation of 2 source pixels contributing to the target pixel, (b) Case B (middle diagram) shows the exception of 1 source pixel contributing to the target pixel and (c) "No-Overlap" Case (right diagram) shows the special situation of the 0th BD3 target pixel present in TROPOMI.

$$\gamma[i] = \frac{H_c^{UV}[i] - H_c^{NIR}[j+1]}{H_c^{NIR}[j] - H_c^{NIR}[j+1]} \quad (13)$$

Then, the cloud-top height at the target pixel is expressed as:

$$Z_c^{UV}[i] = \gamma[i] Z_c^{NIR}[j] + (1 - \gamma[i]) Z_c^{NIR}[j+1]. \quad (14)$$

245 The upper mathematical expressions are valid along the scanline. However, for every sensor there might be exceptions and thus adaptations. For TROPOMI, such exceptions can be spotted from Fig. 2 at (a) BD3 target pixel 21, which is fully covered by the BD6 source pixel 19 (see also Fig. 1), (b) BD3 target pixel 1, where there is partial overlap with the BD6 source pixel 0, and (c) BD3 target pixel 0, where there is no overlap with any source pixel (see also Fig. 6). The first two exceptions fall into Case B of Fig. 5 and follow the mathematical formulations from Equations 8 and 9:

250
$$\gamma[i] = \frac{H_c^{UV}[i]}{H_c^{NIR}[j]}. \quad (15)$$

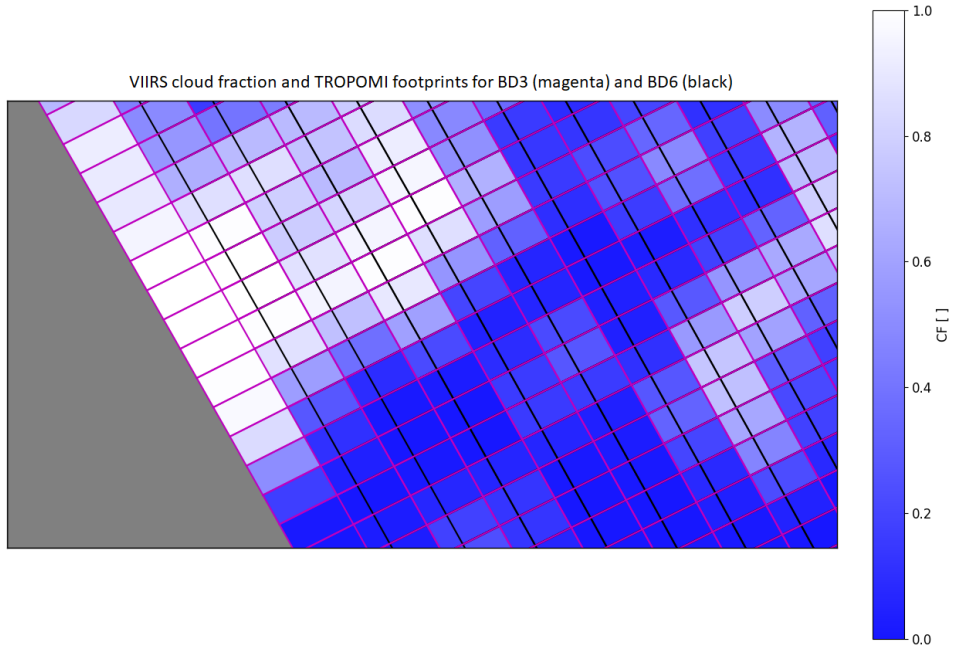


Figure 6. TROPOMI ground pixels for Bands 3 and 6 at the west edge of the orbit. Provided that the mis-match is only in the across-track direction, the horizontal magenta lines of BD3 overlap with the horizontal black lines of BD6.

$$Z_c^{UV}[i] = \gamma[i] Z_c^{NIR}[j]. \quad (16)$$

The last exception of the BD3 target pixel 0 has been treated independently since there is lack of overlap between the BD6 source and BD3 target pixels. A graphical illustration of this scenario is shown in "No-Overlap" Case of Fig. 5. The cloud information from VIIRS imager can be used for the reconstruction of the cloud parameters at the S5P BD3 target pixel 0. The basic principle is that VIIRS and TROPOMI cloud data are interconnected and therefore, each point from the VIIRS dataset can be mapped to the respective TROPOMI point. The adjacent 15 pairs $(H_c^{UV}[i], Z_c^{UV}[i])$, $i \in [2, 17]$ are used to create the mapping function:

$$Z_c^{UV} = f_{z_c}(H_c^{UV}) \approx \alpha H_c^{UV} + \beta \quad (17)$$

The mapping function for the cloud-top height f_{z_c} can be well approximated with a linear regression model. Therefore, first the mapping function is found for each scanline and then the value at the target pixel 0 is estimated as $Z_c^{UV}[i=0] = f_{z_c}(H_c^{UV}[i=0])$. One example scene of the TROPOMI BD3 target pixel 0 is shown in Fig. 7 where it is shown that the "No-Overlap" approach does not introduce inconsistencies or outliers. Notice that since this additional information for TROPOMI BD3 target pixel 0 originates from the VIIRS instrument but scaled to TROPOMI values, the quality of the data depends on how accurately the VIIRS/TROPOMI mapping functions have been constructed. This particularity is reflected into the QA (Quality Assurance) value scheme by adding a penalty for the first TROPOMI BD3 ground pixel (Loyola et al., 2023).

The co-registration of the other ROCINN parameters at the target pixel 0 is possible after finding the mapping function f_{A_c} and f_{τ_c} for the cloud albedo and cloud optical thickness, respectively. Those functions are approximated with the use of one linear and one logarithmic model (Loyola et al., 2023).

4 Application to TROPOMI/S5P with collocated VIIRS/Suomi-NPP data

The new approach has been evaluated using several means of comparison and validation. The VIIRS product has been re-gridded to the TROPOMI ground pixels for the following six test days: 2018-09-09 (orbits 04691-04704), 2019-09-11 (orbits 09898-09911), 2020-09-11 (orbits 15091-15104), 2020-09-26 (orbits 15303-15316), 2021-04-11 (orbits 18098-18111) and 2021-09-11 (orbits 20269-20282).

4.1 Evaluation of the new approach

The new approach has been applied on top of the old scheme to ensure that the co-registration is still performed with the static mapping tables when there are no VIIRS data available. The new scheme is in principle not applicable on the following situations: (a) when TROPOMI or VIIRS pixels contain fill values, (b) when the neighboring VIIRS pixels contain equal values, leading to numerical errors at the weight calculations, (c) when the weight calculation results in values outside the expected range. Another special case, where the new approach for the CF co-registration is not applicable, is when all three VIIRS BD3 pixels are equal $M_c^{UV}[j-1] = M_c^{UV}[j] = M_c^{UV}[j+1]$, while S5P BD3 pixels are different $f_c^{UV}[j-1] \neq f_c^{UV}[j] \neq f_c^{UV}[j+1]$. The combination of both schemes ensures that the cloud product contains as many data as possible.

4.1.1 Overview of comparisons between the two schemes

Note that OCRA cloud fraction must be co-registered to NIR with the fallback for VIIRS fully cloudy scenes (i.e., when VIIRS cloud fraction at both BD3 and BD6 is equal to 1). Therefore, the VIIRS-based scheme is expected to be used for the co-registration of the OCRA cloud fraction in about 30% frequency. The average frequency differs slightly from day to day but it can be considered rather stable when there is VIIRS data availability. The co-registration from NIR to UVIS for the ROCINN parameters is performed with the new scheme with an average frequency of about 70% for the ROCINN CAL cloud-top height (same applies to ROCINN CRB cloud height) and with an average frequency of about 55% for the ROCINN CAL cloud optical thickness (same applies to ROCINN CRB cloud albedo). As seen from the co-registration flag of the ROCINN

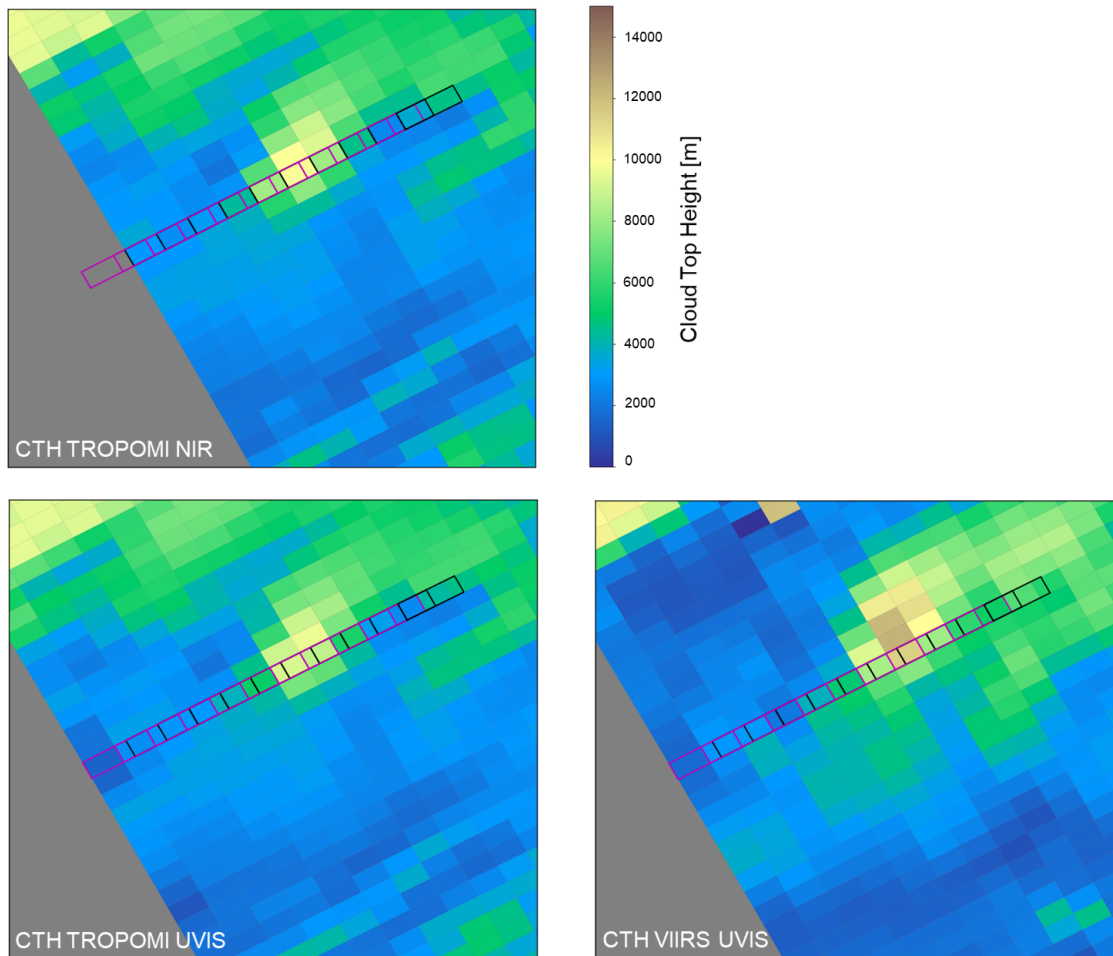


Figure 7. Co-registration of ROCINN Cloud Height from BD6 to BD3 using VIIRS first pixel: example scene. Ground pixels in the source NIR band are indicated with the black frames and the UVIS ground pixels are highlighted with the magenta frames. Notice that (a) the CTH TROPOMI NIR (original parameter) does not contain values in the first magenta ground pixel and (b) the co-registered CTH TROPOMI UVIS and original CTH TROPOMI NIR maps are very similar, demonstrating that the new co-registration scheme does not introduce inconsistencies. Compare visually the CTH TROPOMI and CTH VIIRS in UVIS and observe that the cloud top height values can be very different in absolute numbers but the new co-registration scheme does not alter the original cloud structures.

290 CAL cloud optical thickness in Fig.8 (same applies to ROCINN CRB cloud albedo), the new scheme is only applicable up to a certain latitude and the pixels around the poles are co-registered with the fallback. The only reason for this limitation is that the VIIRS cloud optical thickness originates from the CloudDCOMP EDR (see Section 3.3) which does not contain valid points in high latitudes.

295 Figures 9, 10, 11, 12 and 13 present the scatter between the old and new approach for the co-registered parameters, after the mapping and without any filtering, for one of the days. High correlation coefficients are found for all cloud parameters. For

co-registration flag for ROCINN CAL Cloud Optical Thickness from NIR to UVIS

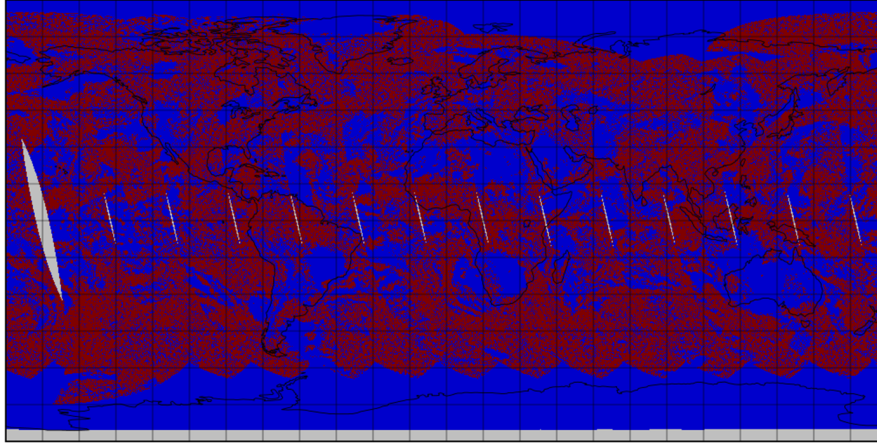


Figure 8. RB color global maps presenting the co-registration flag of day 2018-09-09 for the ROCINN CAL cloud optical thickness: Red color shows the co-registration with the use of VIIRS data and Blue color shows the co-registration with the fallback. The new scheme is applicable for the ROCINN CAL cloud optical thickness for about 55% of the total pixels.

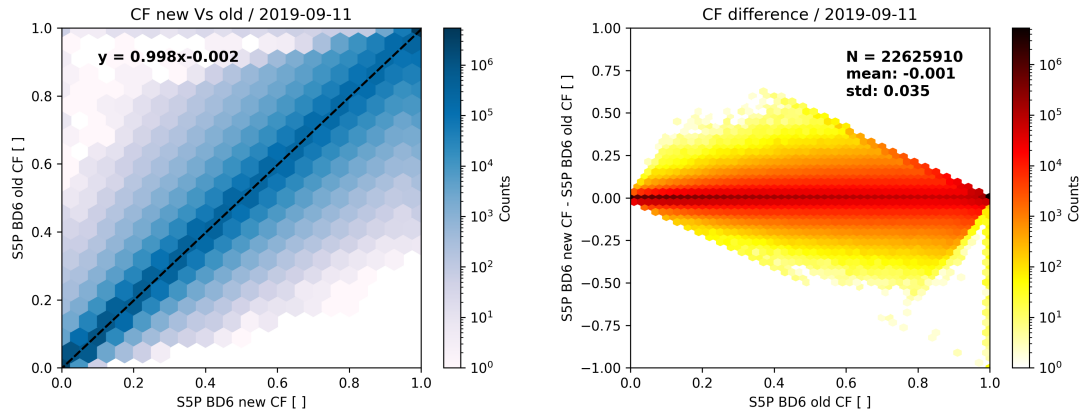


Figure 9. The co-registered cloud fraction for the new versus the old scheme: analysis refers to 22625910 number of pixels without applying any filtering for the day 2019-09-11. The CF scatter plot (left panel) shows the co-registered new $f_c^{\text{NIR}_{\text{new}}}$ in the x-axis versus the co-registered old $f_c^{\text{NIR}_{\text{old}}}$ in the y-axis. The CF difference scatter plot (right panel) shows the CF difference $\Delta f_c = f_c^{\text{NIR}_{\text{new}}} - f_c^{\text{NIR}_{\text{old}}}$ in the x-axis versus the old cloud fraction $f_c^{\text{NIR}_{\text{old}}}$ in the y-axis.

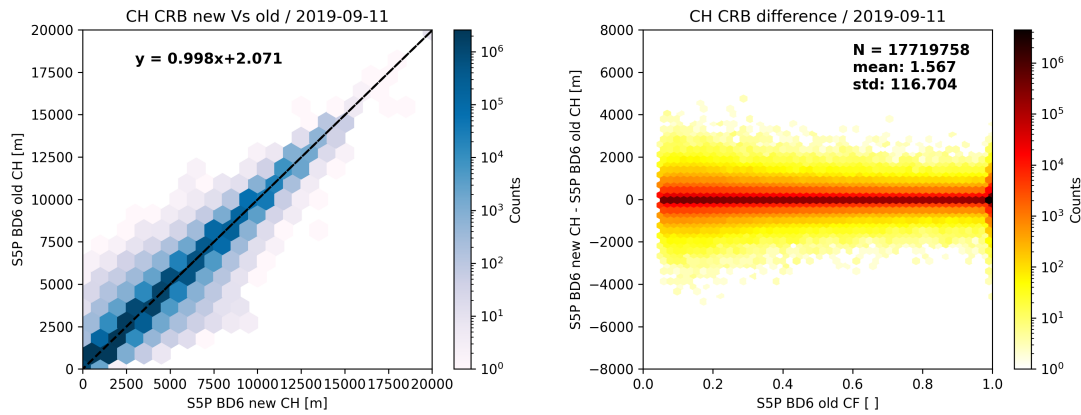


Figure 10. The co-registered ROCINN CRB cloud height for the new versus the old scheme: analysis refers to 17719758 number of pixels without applying any filtering for the 2019-09-11. The CH CRB scatter plot (left panel) shows the co-registered new $Z_c^{UV_{new}}$ in the x-axis versus the co-registered old $Z_c^{UV_{old}}$ in the y-axis. The CH CRB difference scatter plot (right panel) shows the CH difference $\Delta Z_c = Z_c^{UV_{new}} - Z_c^{UV_{old}}$ in the x-axis versus the old cloud fraction $f_c^{NIR_{old}}$ in the y-axis. Notice that there are no data points below $f_c^{NIR_{old}} < 0.05$ as this is considered the lower threshold for ROCINN CBR triggering.

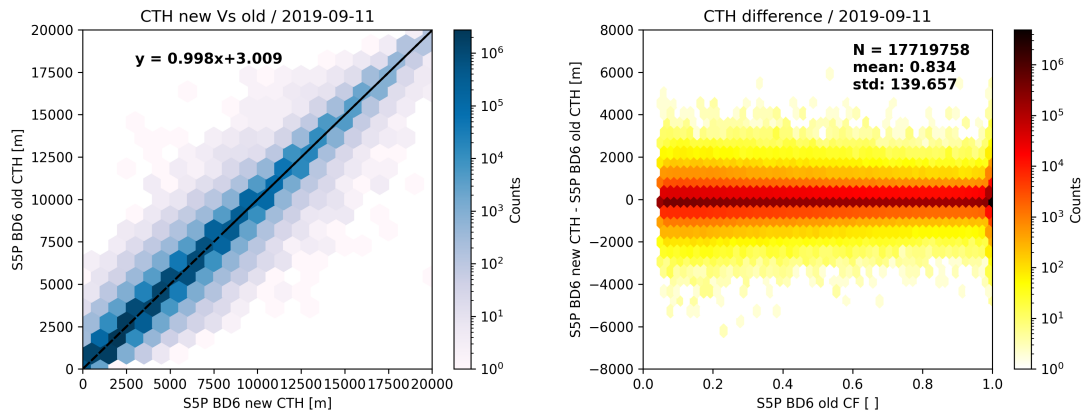


Figure 11. The co-registered ROCINN CAL cloud-top height for the new versus the old scheme: analysis refers to 17719758 number of pixels without applying any filtering for the 2019-09-11. The CTH scatter plot (left panel) shows the co-registered new $Z_c^{UV_{new}}$ in the x-axis versus the co-registered old $Z_c^{UV_{old}}$ in the y-axis. The CTH difference scatter plot (right panel) shows the CTH difference $\Delta Z_c = Z_c^{UV_{new}} - Z_c^{UV_{old}}$ in the x-axis versus the old cloud fraction $f_c^{NIR_{old}}$ in the y-axis. Notice that there are no data points below $f_c^{NIR_{old}} < 0.05$ as this is considered the lower threshold for ROCINN CAL triggering.

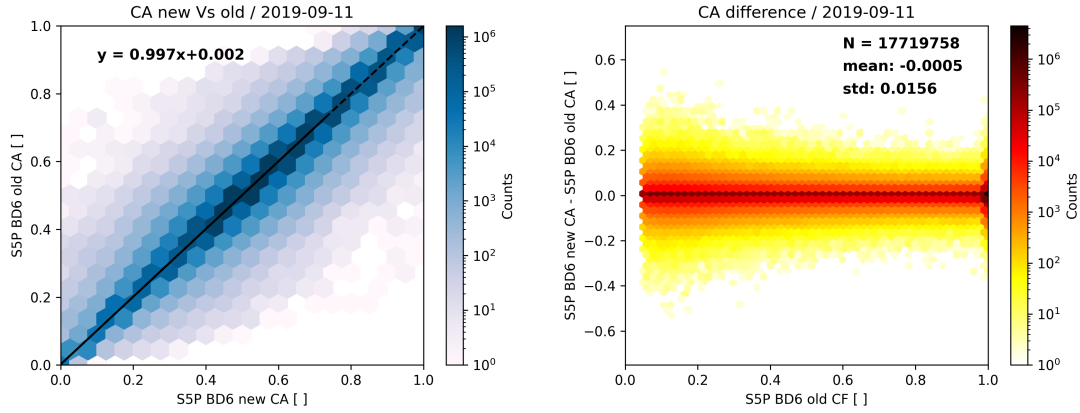


Figure 12. The co-registered ROCINN CRB cloud albedo for the new versus the old scheme: analysis refers to 17719758 number of pixels without applying any filtering for the 2019-09-11. The CA scatter plot (left panel) shows the co-registered new $A_c^{UV_{new}}$ in the x-axis versus the co-registered old $A_c^{UV_{old}}$ in the y-axis. The CA difference scatter plot (right panel) shows the CA difference $\Delta A_c = A_c^{UV_{new}} - A_c^{UV_{old}}$ in the x-axis versus the old cloud fraction $f_c^{NIR_{old}}$ in the y-axis. Notice that there are no data points below $f_c^{NIR_{old}} < 0.05$ as this is considered the lower threshold for ROCINN CRB triggering.

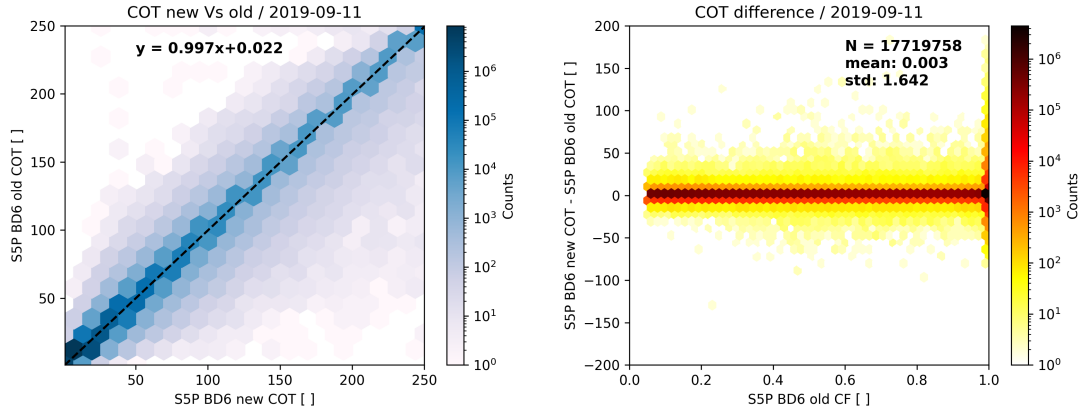


Figure 13. The co-registered ROCINN CAL cloud optical thickness for the new versus the old scheme: analysis refers to 17719758 number of pixels without applying any filtering for the 2019-09-11. The COT scatter plot (left panel) shows the co-registered new $\tau_c^{UV_{new}}$ in the x-axis versus the co-registered old $\tau_c^{UV_{old}}$ in the y-axis. The COT difference scatter plot (right panel) shows the COT difference $\Delta \tau_c = \tau_c^{UV_{new}} - \tau_c^{UV_{old}}$ in the x-axis versus the old cloud fraction $f_c^{NIR_{old}}$ in the y-axis. Notice that there are no data points below $f_c^{NIR_{old}} < 0.05$ as this is considered the lower threshold for ROCINN CAL triggering.

the cloud fraction of Fig. 9, we find that there is less scatter below the identity line than above the identity line. Pixels of fully cloudy conditions (i.e., with cloud fraction 1) in the old scheme have been differentiated in several cases; the cloud fraction obtains lower values with the new scheme as shown at the scatter plot of the CF differences (see right panel in Fig. 9). This means that outliers have been completely or partially removed. For the partly cloudy pixels (i.e., $f_c^{\text{NIRold}} < 1$), some symmetry of the Δf_c differences is observed. The cloud height CRB and cloud-top height CAL are scattered symmetrically around the identity line as can be seen from Figs. 10 and 11, respectively. Notice that the density of data points above 15 km for CH CRB is significantly reduced compared to the respective CTH from ROCINN CAL model. This is expected due to the different cloud model definitions (i.e., ROCINN CRB versus ROCINN CAL) and it is still maintained with the new co-registration. The largest ΔZ_c differences are observed for the small cloud fractions. Likewise for the CA shown in Fig. 12, symmetry around the identity line is observed at the CA scatter plot and the largest ΔA_c differences are observed for the small cloud fractions. On the contrary, some asymmetry is observed at the cloud optical thickness in Fig. 13 with the scatter below the identity line being much higher than the scatter above the line. The respective analysis for the rest of the days lead to similar findings.

The ROCINN CAL absolute differences ΔZ_c between the two co-registration schemes in a global scale are shown in Fig.14. The differences are exactly zero when VIIRS data are not available because the co-registration is done with the fallback. Examples of VIIRS data unavailability (i.e., missing granules or entire orbits) are shown in green ellipsoids on the map. The global maps for the differences of the other cloud parameters support further the following conclusions:

- The differences are not systematically present in certain regions but rather spread everywhere.
- There is not a latitudinal dependence.
- Viewing geometry dependencies are not present.

315 4.1.2 The first westernmost UVIS TROPOMI ground pixel

The use of VIIRS data made possible the reconstruction of cloud information for the first (westernmost) TROPOMI ground pixels in the UVIS grid (see "No-Overlap" case of Fig. 5). The benefit of making use of the VIIRS cloud information to fill in the first UVIS ground pixel is two-fold: (a) the apparent advantage of reducing the "gap" between two adjacent orbits by one ground pixel and (b) the actual retrieval of tropospheric and stratospheric trace gases which require the knowledge of cloud parameters. The data gaps between two adjacent orbits are expected around the equator because the Earth has its maximum circumference there. The effect is a combination of the limitations of TROPOMI swath width together with the inclination and altitude of S5P satellite's orbit. With the new co-registration scheme, those gaps are decreased by approximately 15 km after the addition of meaningful cloud data in the first UVIS ground pixel (see Fig. 15). The approach seems to work smoothly for all cloud types since the cloud heights of the first UVIS ground pixels are well harmonized with the neighboring ones. Similar conclusions can be drawn for all the rest cloud parameters.

The air mass factor (AMF) calculation was evaluated for the total vertical column densities (VCDs) of formaldehyde (HCHO), ozone (O_3), and sulfur dioxide (SO_2) in the first UVIS ground pixel. The plot in Fig. 16 depicts the total verti-

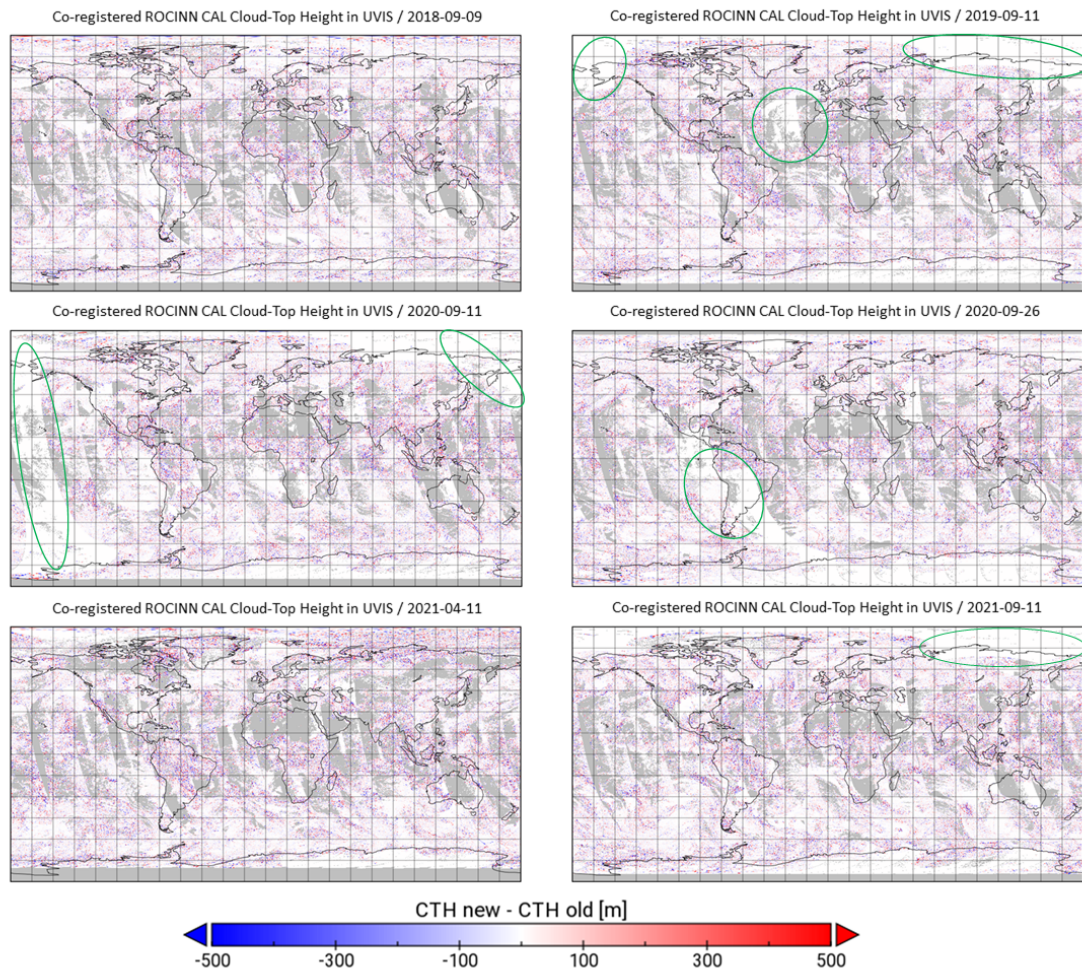


Figure 14. Daily global maps with comparisons between the two co-registration schemes: the ROCINN CAL absolute differences ΔZ_c in the UVIS grid are shown for the six available days.

cal column of ozone, where in most cases we see an additional column of O_3 data and the data agree very well with the neighboring column. This smooth transition is found for all cloud fractions, as shown in Fig. 17. In the selected area, there are
 330 cloudy and cloud free pixels, as well as partly cloudy pixels. Even in the partly cloudy pixels, the O_3 columns agree well with the neighboring ones. For HCHO and SO_2 retrievals, the VCDs look smooth and reasonable for this additional row. For SO_2 , the detection algorithm could even identify elevated VCDs at the first row and flag them with volcanic origin. In Fig. 18, we can see the SO_2 column densities after the Sierra Negra volcanic eruption. In the selected area, the pixels from the additional first row highlighted with a red frame have been automatically flagged as "volcanic".

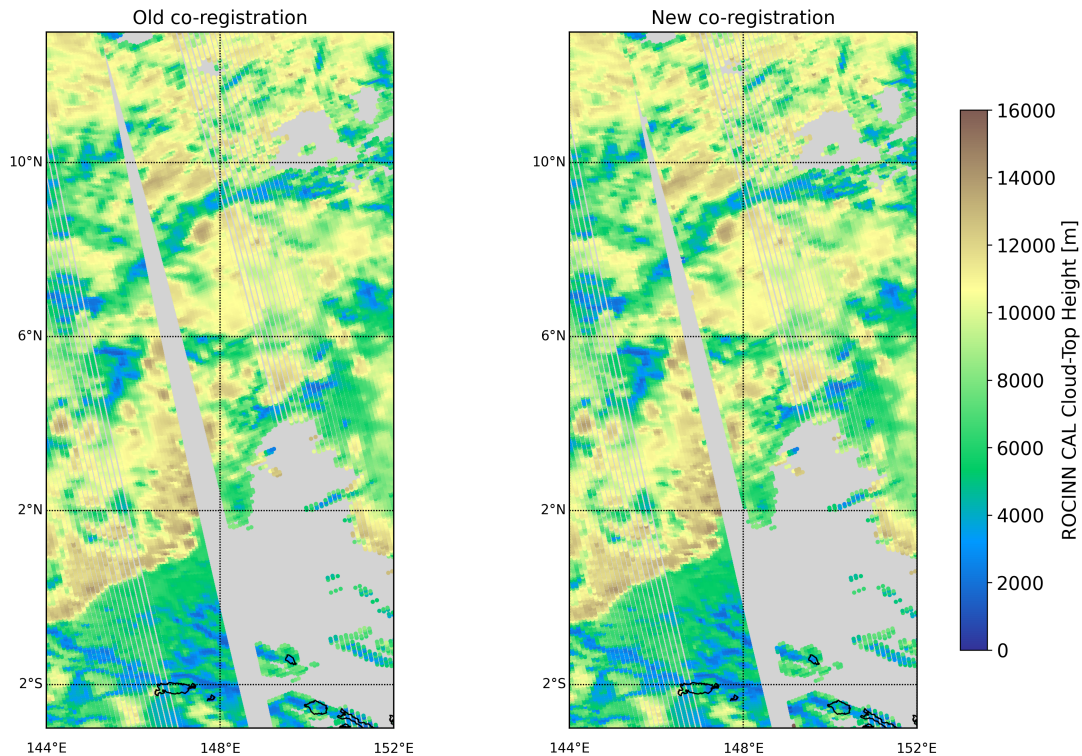


Figure 15. Two adjacent orbits displaying the co-registered cloud-top height at the UVIS grid using the static LUTs (left panel: "Old co-registration") versus using VIIRS data (right panel: "New co-registration"). The gaps between the adjacent orbits are reduced with the addition of meaningful cloud data at the first UVIS ground pixels.

335 4.2 Further evaluation in the across-track flight direction

An extensive investigation of the co-registration scheme impact on the cloud fraction in the across-flight direction has been performed. As expected, the major improvements have been identified at heterogeneous scenes in the vicinity of local minima and maxima. Usually, the co-registered value is closer to the one retrieved at the original band when using the new scheme. So far, we have seen that the co-registration process with the static mapping tables tends to smooths out structure which appears initially at the original band. When the co-registration is done based on the VIIRS data, the cloud structure is maintained simply because it is captured by the VIIRS-based weighting factors. The co-registration impact can be larger in inhomogeneous scenes with relatively small cloud fractions; a small fluctuation of the cloud fraction at a low cloud fraction results in a large fractional difference. An example of a single scanline at longitude range [-34.7, -34.1] is presented in Fig. 19. The improvement with the new scheme is shown in points A-B-C around longitude -34.5 degree. The OCRA cloud fraction at the original BD3 has the same value at BD6 after the co-registration in point A. In other words, both co-registration schemes agree with the value obtained at the original band. However, the drop of the cloud fraction at point B demonstrates the importance on the

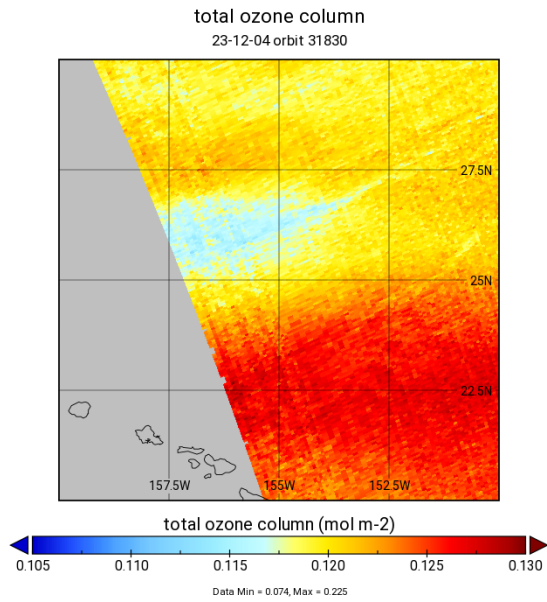


Figure 16. The total ozone column for the scene of Fig. 17. The total ozone column for the first row looks smooth w.r.t. the adjacent rows.

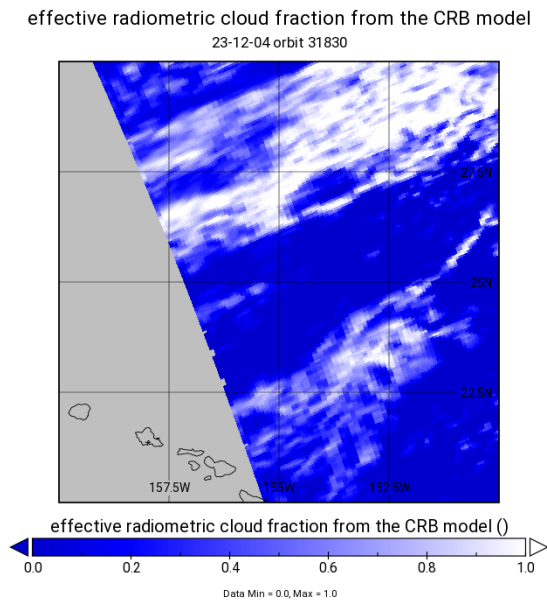


Figure 17. The radiometric cloud fraction from the ROCINN CRB model is used as an input parameter for the cloud correction in the ozone OFFL algorithm.

Sentinel-5 Precursor
19/06/2018
Sierra Negra

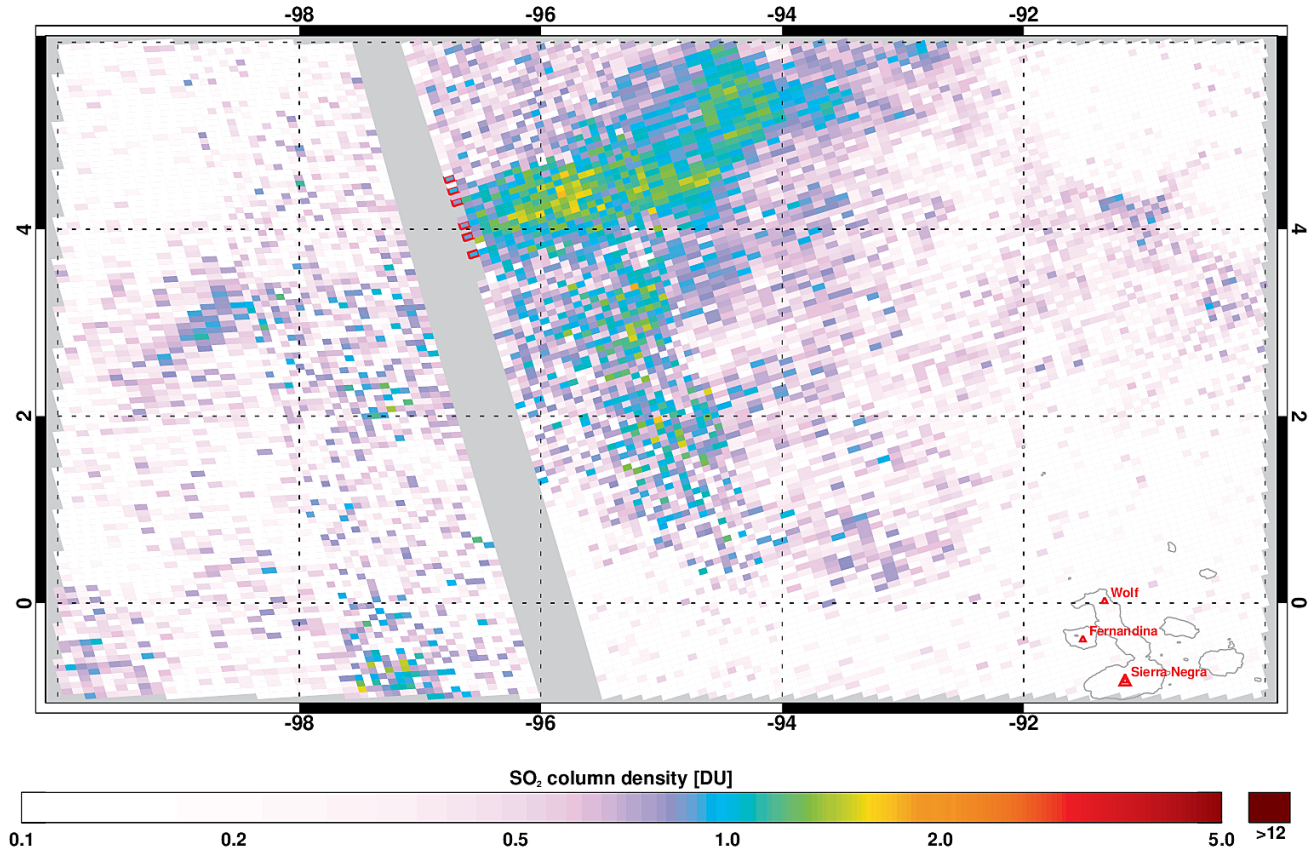


Figure 18. The SO_2 column density for a scene of the Sierra Negra volcanic eruption. Pixels highlighted with the red frames in the first detector row are detected with volcanic origin. The detection algorithm for volcanic SO_2 seems to work well for the additional first row as some pixels are flagged as volcanic.

co-registration scheme selection. The co-registered value obtained with the new scheme at point B is closer to the original one of BD3 than with the old scheme. In Table 3, an absolute difference of 0.04 is found between the two schemes, which at first does not seem significant. However, due to the low original cloud fraction of 0.13, a fractional difference of 30% seems to be introduced just by using a different co-registration. **Another important aspect at point B** is that the cloud fraction gets below 0.2 with the new scheme. A cloud fraction of 0.2 is usually considered the cut-off threshold of clear sky versus partially cloudy to obtain clear sky series of tropospheric trace-gas concentrations (Liu et al., 2021). The cloud fraction with the old co-registration was 0.21, which would mean that trace-gas retrieval for **point B** will be triggered with the new co-registration scheme. Similar improvement is found at **points D-E-F** between longitude range [-34.3,-34.2]. At **point D**, both co-registered

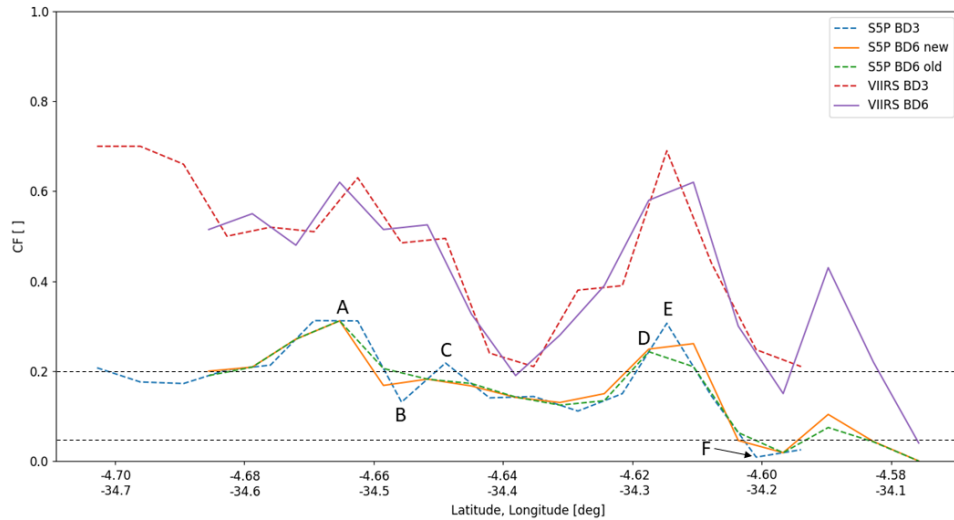


Figure 19. Inhomogeneous scene with low TROPOMI cloud fraction: the new co-registration scheme has a considerable positive effect at local minimum (e.g. points B and F) or maximum (e.g., point E). The data refer to 2020-09-11, orbit 15099, scanline 1820, pixels 268-285.

355 cloud fractions are equal to the original one. But at point E, the new co-registered cloud fraction is 16% lower than the original value. At this point E, when co-registration is done with the old scheme the fractional difference is 32%. Even more interesting is the situation at point F where the original value is extremely low at 0.01. There, the selection of the co-registration scheme will determine the activation of ROCINN algorithm. The new co-registered value is still below 0.05, which is the threshold currently used to continue with the ROCINN retrievals of the remaining cloud parameters. Therefore, the use of VIIRS in the
 360 cloud co-registration process can act as a tool to remove existing cloud outliers.

A second interesting scene with scattered clouds close to the Brazilian Coast line is presented in Fig. 20. At longitude around -36.10, the cloud fraction obtained in BD3 was equal to 0.96. This is a scene over ocean with the effect of sun-glint. An enhanced TROPOMI cloud fraction is generally expected under sun-glint geometry, and this is a possible reason that OCRA cloud fraction is found larger than VIIRS; VIIRS gives a 0.72 cloud fraction in both bands. The old co-registration scheme
 365 moves the cloud fraction closer to VIIRS. Nevertheless, the new co-registration seems to reflect better the original BD3 cloud fraction of 0.96 to a 0.94 BD6 cloud fraction.

Investigation of the co-registration scheme impact on the cloud-top height in the across-flight direction has been done too. In general, similarly to the cloud fraction, the largest impact is shown at the inhomogeneous scenes at the local maxima and minima. At first, the new co-registered cloud-top height is closer to the one obtained with ROCINN CAL at the original BD6
 370 band. Two examples are shown in Fig. 21 at points A and B, with the new co-registered cloud-top height being approximately

Table 3. Cloud fraction values at the original BD3 and the co-registered BD6 with both new and old techniques. The latitudes (first column) and longitudes (second column) refer to points A-B-C-D-E-F of Fig. 19.

Latitude (pixel)	Longitude (pixel)	ORIGINAL BD3	CO-REGISTERED NEW BD6	CO-REGISTERED OLD BD6
-4.667 (A)	-34.53 (A)	0.31	0.31	0.31
-4.655 (B)	-34.48 (B)	0.13	0.17	0.21
-4.649 (C)	-34.44 (C)	0.22	0.18	0.18
-4.617 (D)	-34.29 (D)	0.24	0.24	0.24
-4.612 (E)	-34.25 (E)	0.31	0.26	0.21
-4.602 (F)	-34.21 (F)	0.01	0.04	0.06

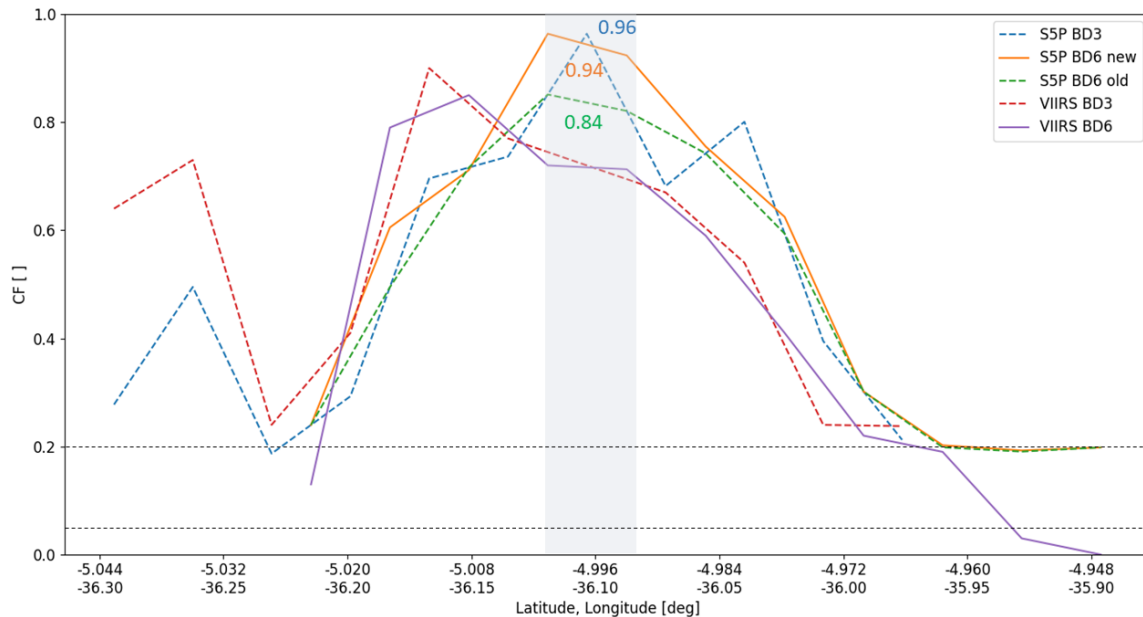


Figure 20. Inhomogeneous scene with high TROPOMI cloud fraction but with small horizontal extend. This could be considered a "single-cloud" scene where the new co-registration is preferable at local maximum because S5P BD6 new cloud fraction agrees better with S5P BD3 cloud fraction. The data refer to 2020-09-11, orbit 15099, scanline 1820, pixels 219-230.

300 m higher than the old co-registered value and in both cases closer to the original values. The cloud-top heights at the original BD6 were 7600 m and 9400 m at points A and B respectively. *After the co-registration, we could approximate the BD3 cloud-top height at point A by taking into account the two contributing pixels: with the old scheme was approximately*

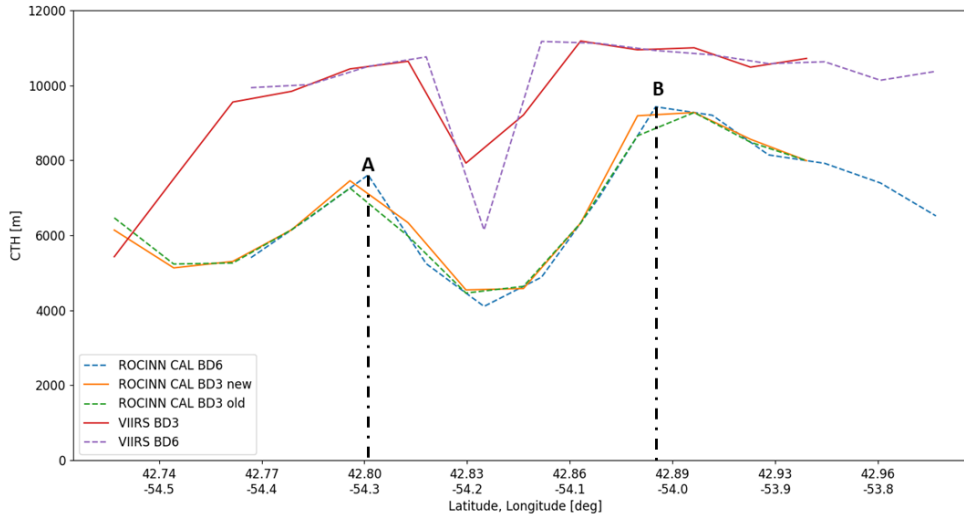


Figure 21. Inhomogeneous scene with two local maxima at points A and B where the new co-registration scheme has a positive impact on the ROCINN CAL CTH at BD3. The data refer to 2020-09-11, orbit 15099, scanline 2820, pixels 107-120.

6600 m (the contributing pixels had CTH values of about 7200 m and 6000 m) and with the new scheme was about 6900 m (the contributing pixels had CTH values of about 7500 m and 6300 m). At point B, the co-registered CTH at BD3 with the new scheme was approximately 9300 m (both contributing pixels had CTH values of about 9300 m) and with the old scheme was about 9000 m (contributing pixels had values of about 8700 m and 9300 m). We see that the advantage of using the VIIRS re-gridded data for the ROCINN cloud height co-registration is that small-scale cloud structures can be introduced back to the TROPOMI UVIS CTHs, while with the old co-registration approach they were smoothed out.

380 4.3 Evaluation in the along-track flight direction: comparisons against CALIPSO overpasses

The evaluation of the new co-registration scheme in the along-track direction for the cloud-top height parameter was done using the independent instrument CALIOP (Cloud-Aerosol Lidar with Orthogonal Polarization) which is part of the CALIPSO (Cloud-Aerosol Lidar and Infrared Pathfinder Satellite Observations) payload. CALIPSO satellite was launched in April 2006 in formation with the CloudSat satellite as part of the A-Train constellation of satellites (Winker et al., 2003, 2004, 2007). For 12 years, it maintained a sun-synchronous orbit with an altitude of 705 km and inclination of 98.2° crossing the equator each day at around 1:30 pm solar time. After September 2018, it was moved to a lower orbit together with CloudSat, part of the C-train approximately 688 km above the Earth's surface (Atkinson, 2018). CALIOP was a two-wavelength (i.e., operating at 532 nm and 1064 nm) polarization-sensitive lidar that provided high-resolution vertical profiles of aerosols and clouds.

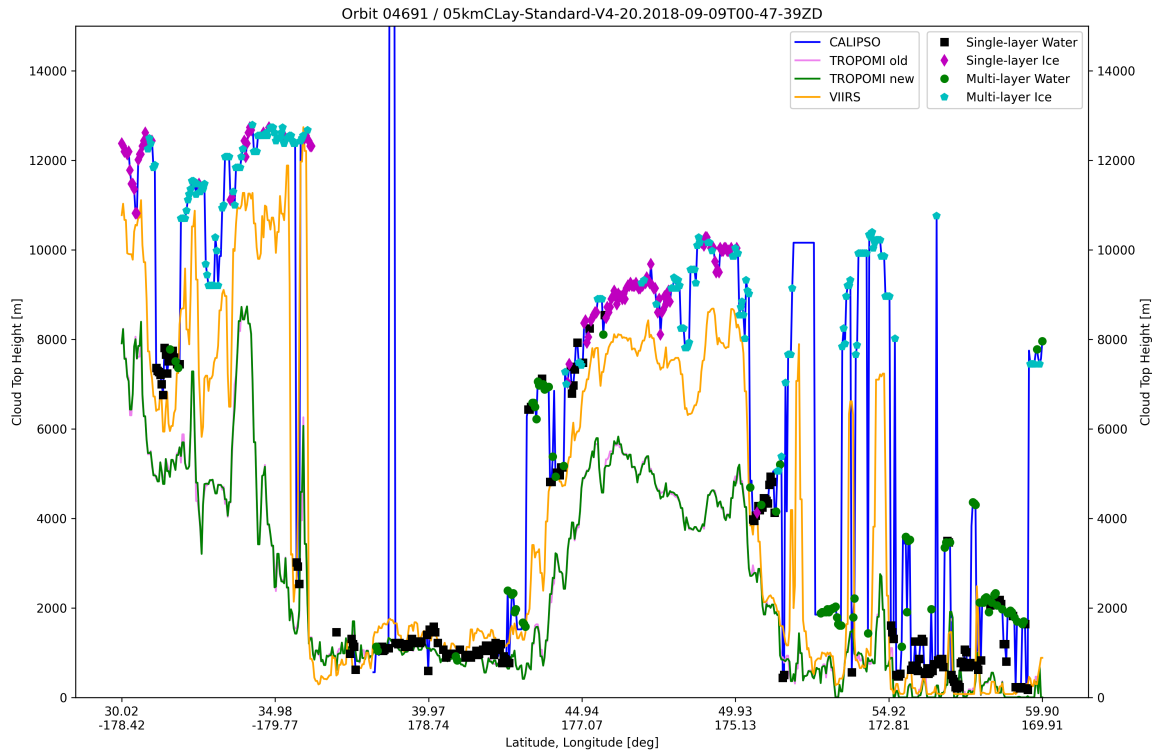


Figure 22. Comparison of the CTH for TROPOMI, VIIRS and CALIPSO for mid-latitudes in the northern hemisphere over the Pacific ocean. The TROPOMI orbit 04691 for day 2018-09-09 is collocated with the CALIPSO measurements from the 2018-09-09T00-47-39ZD overpass.

CALIPSO could identify cloud and aerosol layers down to the level in which the lidar signal was totally attenuated. Frequently, the atmosphere contained multi-layer clouds limiting the lidar capabilities and making the cloud retrievals in such conditions more challenging (Liu et al., 2020). Even though CALIPSO could provide the cloud information with the fine spatial resolution of 1 km, in this study the spatial resolution of 5 km in the Level 2 cloud layer information (Version 4) was used.

CALIPSO overpasses have been collocated to the TROPOMI orbits. The TROPOMI/CALIPSO collocation method is described in the Appendix A. An example comparison at mid-latitudes of the northern hemisphere over the Pacific ocean is presented in Fig. 22. This is quite representative for the comparison between the three instruments. Good agreement between all is seen for the low maritime clouds with a cloud-top height lower than 2 km. For medium and high clouds, we observe differences between TROPOMI and CALIPSO, while those differences should also depend on the phase of the detected clouds. The ice clouds are not well represented in the forward model of TROPOMI and some bias could originate from the mis-treatment of clouds with a liquid water scattering model. Moreover, in TROPOMI we do not have any special treatment for the scenes with multi-layer clouds and this is another source for differences to be expected. Nevertheless, the focus of this study is on the improvements that could arise from the new co-registration scheme alone. Two cases are presented in the following Figs 23 and

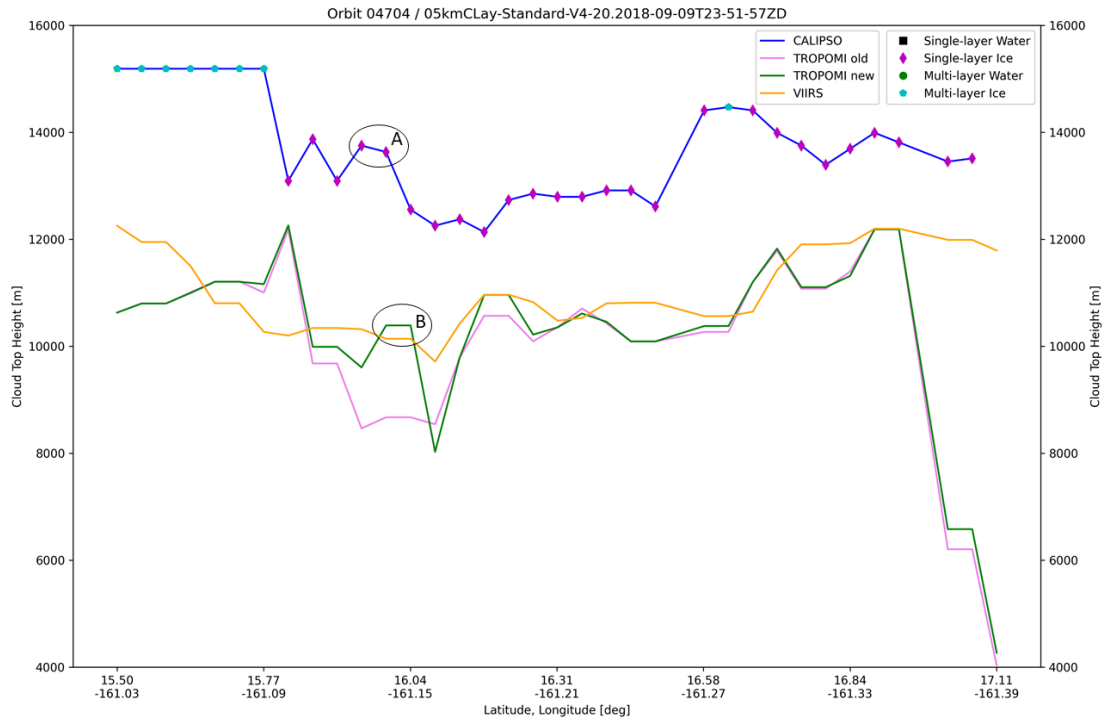


Figure 23. Comparison of the CTH for TROPOMI, VIIRS and CALIPSO for the tropics in the northern hemisphere over the Pacific ocean. The TROPOMI orbit 04704 for day 2018-09-09 is collocated with the CALIPSO measurements from the 2018-09-09T23-51-57ZD overpass.

24. In general, the differences due to the co-registration (comparison between green and pink lines) are small. The largest improvement is seen when the cloud structure, introduced by the use of VIIRS data, results in a better agreement with CALIPSO. In Fig. 23, the small peak (highlighted by the circle A) appearing in the CALIPSO data is seen in the TROPOMI data only when the new co-registration is used. The pink line is flat around 16 deg latitude North, meaning that the old co-registration smooths this cloud structure and the impact on the CTH is an absolute difference of about 2 km compared to the new scheme. Similarly, in another example shown in Fig. 24, there are two peaks (A and B) around 15.5 deg latitude North in the CALIPSO data. None of them is present in the TROPOMI data with the old co-registration (pink line). When the new scheme is used, the peak C appears approximately at the same latitude with CALIPSO peak B. At point C, the absolute difference between the two co-registration methods is approximately 800 m.

5 Conclusions

The existence of collocated cloud information from VIIRS allowed the improvement of TROPOMI cloud properties through a better treatment of the spatial mis-alignment between UVIS and NIR ground pixels. The new scheme is applied on top of the old

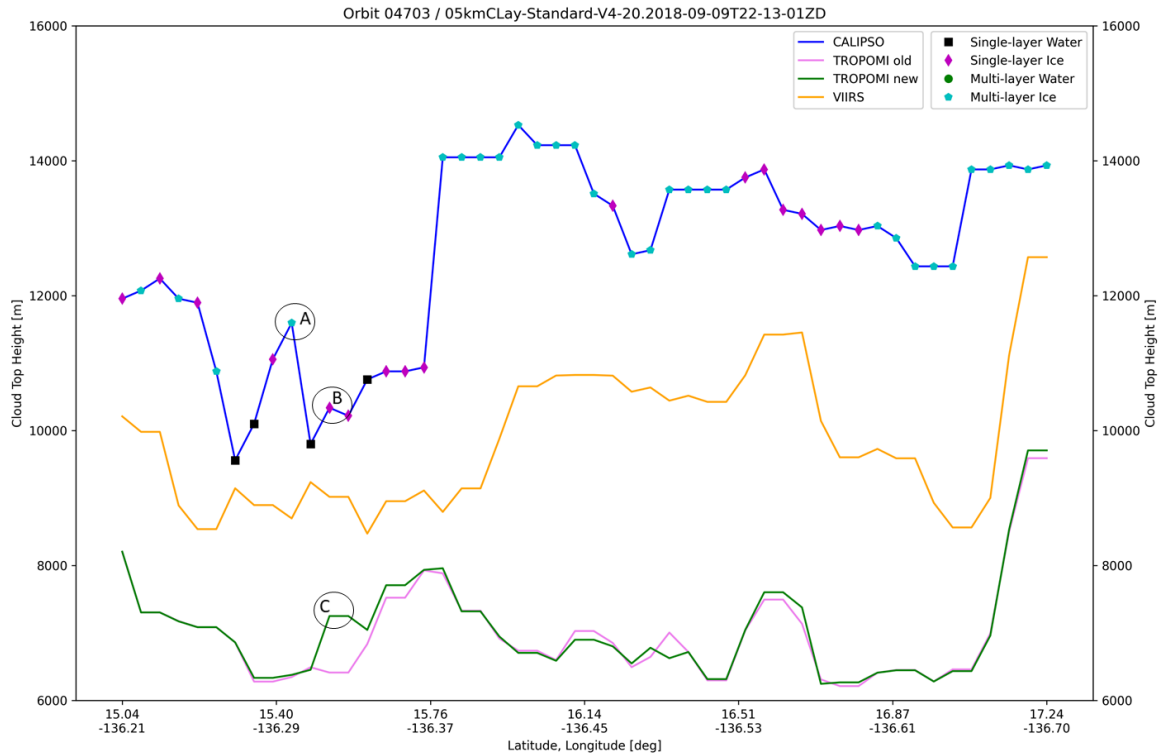


Figure 24. Comparison of the CTH for TROPOMI, VIIRS and CALIPSO for the tropics in the northern hemisphere over the Pacific ocean. The TROPOMI orbit 04703 for day 2018-09-09 is collocated with the CALIPSO measurements from the 2018-09-09T22-13-01ZD overpass.

static mapping tables. The improvement on the TROPOMI data quality together with the optimizations of the co-registration
415 scheme are summarized in the following bullets:

- From the daily scatter plots, we saw that under fully cloudy conditions (i.e., with cloud fraction 1 in the old scheme) the co-registered cloud fraction obtains lower values with the new co-registration scheme. Moreover, several partly cloudy pixels have been characterized as cloud-free with the new co-registration scheme. **Therefore, the new scheme can be effective in removing some outliers.** The ROCINN CRB cloud height and CAL cloud-top height are scattered
420 symmetrically around the identity line, while some asymmetry is observed at the cloud optical thickness with the scatter below the identity line being much higher than the scatter above the line.
- **The largest cloud height differences between the two co-registration schemes were found for the lower cloud fractions over inhomogeneous scenes.**
- From the daily global maps showing the differences between the two schemes, we excluded systematic differences
425 present in certain geographical regions. In addition, we haven't found any latitudinal or viewing geometry dependency.

- The cloud information from the complementary sensor (e.g., VIIRS for the TROPOMI co-registration) allows the reconstruction of the ROCINN retrieved parameters on the first westernmost UVIS ground pixel. The addition of this first pixel had primarily reduced the existing gaps between two adjacent orbits around the equator. Moreover, column information of UVIS trace gases is successfully retrieved for this first pixel, with a positive initial feedback for the accuracy of those retrievals for total ozone and tropospheric SO₂. An example scene in a day with a volcanic eruption showed that the detection algorithm for flagging SO₂ pixels with volcanic origin seems to work well for the additional first ground pixels.
 - From the validation of TROPOMI against VIIRS in the across-track flight direction, the general conclusion is that the old co-registration scheme tends to smooth out local maxima and minima along the scanline. This is quite important finding because the original cloud parameter loses some structure which could be re-constructed through the use of the VIIRS data. This finding is valid for the cloud fraction and the cloud-top height.
 - We identified cases where the co-registered value agrees better with the original value at the source band when the new technique is used. This is true for the co-registration of the cloud fraction from UVIS to NIR but also for the cloud-top height co-registered from NIR to UVIS.
 - From the validation exercise of TROPOMI against CALIPSO, we found cases with better agreement with CALIPSO when using the new co-registration scheme. The agreement refers exclusively to the CTH structure in a qualitative manner. Quantitative comparison against CALIPSO CTHs would not be appropriate because there is a systematic bias in TROPOMI CTH associated with the lack of ice cloud parameterization in the forward cloud model and the treatment of multi-layer clouds.
- 445 The new co-registration scheme has been incorporated into the operational processing system for S5P. The latest UPAS processor version 2.6 has been effective starting from 2023-11-26, orbit 31705. Once S-4 has been launched, a similar approach will be used for the treatment of the spatial mis-registration, using collocated FCI data.

Data availability. The S5P Level-2 CLOUD product refers to UPAS Version 2.4 and can be accessed from the Copernicus Data Space Ecosystem search tool (<https://dataspace.copernicus.eu/>). The S-NPP VIIRS data mapped to the Tropomi grids for band 3, 6, and 7 are also available in the Copernicus Data Space Ecosystem search tool. The re-gridded S5P-NPP cloud data in BD3 and BD6 for the test days are not publicly available since this dataset was explicitly built to support the development of the new co-registration scheme. The L2 cloud layer "CAL_LID_L2_05kmCLay-Standard-V4-20" Version 4-20 data product has been used (NASA/LARC/SD/ASDC, 2018). Data generation and distribution of this V4.20 product ended on July 1, 2020 to support a change in the operating system of the CALIPSO production clusters. The V4.21 data product covers July 1, 2020, to June 30, 2023.



Figure A1. TROPOMI ground pixels at BD3 grid (black color) and CALIPSO overpass measurements (red color). One or even two CALIPSO data points can fall into the TROPOMI BD3 ground pixel. Every TROPOMI ground pixel contains two numbers; the first refers to the scanline and the second to the pixel id. The CALIPSO measurements are identified directly with the geographic coordinates.

455 **Appendix A: Collocation method for TROPOMI and CALIPSO**

Fig. A1 visualizes the CALIPSO overpass measurements within the TROPOMI ground pixels in BD3 grid. The TROPOMI/CALIPSO collocation method is based on finding the smallest distance d_{\min} between a CALIPSO measurement and the center of TROPOMI ground pixel in the vicinity of CALIPSO measurement. The following computational steps are performed:

- The CALIPSO latitude (ϕ_C) and longitude (λ_C) coordinates define the search grid with a step of 0.1° in the latitude dimension and 0.05° in the longitude dimension.
- For every TROPOMI ground pixel within the search window $[\phi_C - 0.1, \phi_C + 0.1]$, $[\lambda_C - 0.05, \lambda_C + 0.05]$, the distances d_C between the CALIPSO geographic coordinates and the center coordinates of each TROPOMI ground pixel (ϕ_T, λ_C) are calculated based on Equation A1.

$$d_C = 2 \operatorname{atan}2(\sqrt{\alpha}, \sqrt{1-\alpha}) R, \quad (\text{A1})$$

465 where R is the Earth's radius ($R = 6378137$ m at the equator). Define as $\Delta\phi = \operatorname{rad}(\phi_T - \phi_C)$ and $\Delta\lambda = \operatorname{rad}(\lambda_T - \lambda_C)$ the difference of geographic coordinates between TROPOMI and CALIPSO. Then, the α parameter of Equation A1 can be

calculated as:

$$\alpha = \left(\sin \frac{\Delta\phi}{2} \right)^2 + \left(\sin \frac{\Delta\lambda}{2} \right)^2 \cos(\text{rad}(\phi_T)) \cos(\text{rad}(\phi_C)). \quad (\text{A2})$$

- 470 – Finally, the TROPOMI ground pixel with the smallest distance $d_{\min} = \min(|d_C|)$ w.r.t. the CALIPSO measurement is accepted as the most successful collocation between the two instruments.

Author contributions. AA, RL and DL developed the conceptual approach of the new co-registration scheme. AA implemented the co-registration prototype algorithm in Python. FR incorporated the prototype algorithm into the operational UPAS system. For TROPOMI, RL was responsible for the development of the prototype OCRA algorithm. AA and VMG were responsible for the development of the prototype ROCINN cloud retrieval algorithm. RS developed the S5P-NPP processor and provided the VIIRS re-gridded data. AA performed
475 the analysis of the impact of the new algorithm on the cloud parameters based on the comparison of the available datasets from VIIRS and CALIPSO. K-PH and PH studied the impact of the new scheme on total ozone column and SO₂, respectively. AA prepared the manuscript with contributions from all co-authors.

Competing interests. The authors have the following competing interests: [One of the \(co-\)authors](#) is a member of the editorial board of Atmospheric Measurement Techniques.

480 *Acknowledgements.* We would like to thank Rob Spurr for his continuous support on LIDORT. In addition, we thank our colleagues from the Royal Belgian Institute for Space Aeronomy (BIRA-IASB) Michel Van Roozendael, Jeroen Van Gent and Nicolas Theys for their support on the O₃ GODFit and SO₂ data. Moreover, we thank all the former and current DLR colleagues who contributed to the algorithm development in the UPAS system. We also acknowledge DLR internal S5P project (KTR 2472046) for financing the algorithm development, ESA ATM-MPC and ESA S5P PDGS projects for financing the operational implementation.

485 References

- Atkinson, J.: Sister Satellites, Briefly Separated, Working Together Again, <https://www.nasa.gov/feature/langley/sister-satellites-briefly-separated-working-together-again>, accessed: 2023-03-13, 2018.
- Bohren, C. F. and Huffman, D. R.: Absorption and scattering by small particles, Wiley, NY, 1983.
- Cahalan, R. F., Ridgway, W., Wiscombe, W. J., Gollmer, S., and Harshvardhan: Independent Pixel and Monte Carlo Estimates of Stratocumulus Albedo, *Journal of Atmospheric Sciences*, 51, 3776–3790, [https://doi.org/10.1175/1520-0469\(1994\)051<3776:IPAMCE>2.0.CO;2](https://doi.org/10.1175/1520-0469(1994)051<3776:IPAMCE>2.0.CO;2), 1994.
- 490 Chambers, L. H., Wielicki, B. A., and Evans, K. F.: Accuracy of the independent pixel approximation for satellite estimates of oceanic boundary layer cloud optical depth, *Journal of Geophysical Research: Atmospheres*, 102, 1779–1794, <https://doi.org/10.1029/96JD02995>, 1997.
- 495 Compernelle, S., Argyrouli, A., Lutz, R., Sneep, M., Lambert, J.-C., Fjæraa, A. M., Hubert, D., Keppens, A., Loyola, D., O'Connor, E., Romahn, F., Stammes, P., Verhoelst, T., and Wang, P.: Validation of the Sentinel-5 Precursor TROPOMI cloud data with Cloudnet, Aura OMI O₂-O₂, MODIS, and Suomi-NPP VIIRS, *Atmospheric Measurement Techniques*, 14, 2451–2476, <https://doi.org/10.5194/amt-14-2451-2021>, 2021.
- Cox, C. S. and Munk, W. H.: Measurement of the Roughness of the Sea Surface from Photographs of the Sun's Glitter, *Journal of the Optical Society of America*, 44, 838–850, 1954.
- 500 De Smedt, I., Theys, N., Yu, H., Danckaert, T., Lerot, C., Compernelle, S., Van Roozendaal, M., Richter, A., Hilboll, A., Peters, E., Pedergnana, M., Loyola, D., Beirle, S., Wagner, T., Eskes, H., van Geffen, J., Boersma, K. F., and Veefkind, P.: Algorithm theoretical baseline for formaldehyde retrievals from S5P TROPOMI and from the QA4ECV project, *Atmospheric Measurement Techniques*, 11, 2395–2426, <https://doi.org/10.5194/amt-11-2395-2018>, 2018.
- 505 Heidinger, A. and Straka, W.: Algorithm Theoretical Basis Document For NOAA Enterprise Cloud Mask, Version 1.2, https://www.star.nesdis.noaa.gov/jpss/documents/ATBD/ATBD_EPS_Cloud_Mask_v1.2.pdf, 2020.
- Heidinger, A., Li, Y., and Wanzong, S.: Algorithm Theoretical Basis Document For Enterprise AWG Cloud Height Algorithm (ACHA), Version 3.4, https://www.star.nesdis.noaa.gov/jpss/documents/ATBD/ATBD_EPS_Cloud_ACHA_v3.4.pdf, 2020.
- Heidinger, A. K., Evan, A. T., Foster, M. J., and Walther, A.: A Naive Bayesian Cloud-Detection Scheme Derived from CALIPSO and Applied within PATMOS-x, *Journal of Applied Meteorology and Climatology*, 51, 1129 – 1144, <https://doi.org/10.1175/JAMC-D-11-02.1>, 2012.
- 510 Heue, K.-P., Eichmann, K., and Valks, P.: TROPOMI/S5P ATBD of tropospheric ozone data products, Tech. Rep. S5P-L2-IUP-ATBD-400C, issue 1.6, Deutsches Zentrum für Luft- und Raumfahrt e.V. in der Helmholtz Gemeinschaft and Institute for Environmental Physics (IUP), <https://sentinel.esa.int/documents/247904/2476257/Sentinel-5P-ATBD-TROPOMI-Tropospheric-Ozone>, 2018.
- 515 King, M. D.: Determination of the Scaled Optical Thickness of Clouds from Reflected Solar Radiation Measurements, *Journal of Atmospheric Sciences*, 44, 1734–1751, [https://doi.org/10.1175/1520-0469\(1987\)044<1734:DOTSOT>2.0.CO;2](https://doi.org/10.1175/1520-0469(1987)044<1734:DOTSOT>2.0.CO;2), 1987.
- Kleipool, Q., Ludewig, A., Babić, L., Bartstra, R., Braak, R., Dierssen, W., Dewitte, P.-J., Kenter, P., Landzaat, R., Leloux, J., Loots, E., Meijering, P., van der Plas, E., Rozemeijer, N., Schepers, D., Schiavini, D., Smeets, J., Vacanti, G., Vonk, F., and Veefkind, P.: Pre-launch calibration results of the TROPOMI payload on-board the Sentinel-5 Precursor satellite, *Atmospheric Measurement Techniques*, 11, 6439–6479, <https://doi.org/10.5194/amt-11-6439-2018>, 2018.
- 520

- KNMI: S5P/TROPOMI Algorithm theoretical basis document for the TROPOMI L01b data processor, S5P-KNMI-L01B-0009-SD, issue 10.0.0, 2022.
- Kokhanovsky, A. A. and Mayer, B.: Light reflection and transmission by non-absorbing turbid slabs: simple approximations, *Journal of Optics A: Pure and Applied Optics*, 5, 43–46, <https://doi.org/10.1088/1464-4258/5/1/306>, 2003.
- 525 Latsch, M., Richter, A., Eskes, H., Sneep, M., Wang, P., Veefkind, P., Lutz, R., Loyola, D., Argyrouli, A., Valks, P., Wagner, T., Sihler, H., van Roozendaal, M., Theys, N., Yu, H., Siddans, R., and Burrows, J. P.: Intercomparison of Sentinel-5P TROPOMI cloud products for tropospheric trace gas retrievals, *Atmospheric Measurement Techniques*, 15, 6257–6283, <https://doi.org/10.5194/amt-15-6257-2022>, 2022.
- Liu, C.-Y., Chiu, C.-H., Lin, P.-H., and Min, M.: Comparison of cloud-top property retrievals from Advanced Himawari Imager, MODIS, CloudSat/CPR, CALIPSO/CALIOP, and radiosonde, *Journal of Geophysical Research: Atmospheres*, 125, e2020JD032683, <https://doi.org/10.1029/2020JD032683>, 2020.
- 530 Liu, S., Valks, P., Pinardi, G., Xu, J., Chan, K. L., Argyrouli, A., Lutz, R., Beirle, S., Khorsandi, E., Baier, F., Huijnen, V., Bais, A., Donner, S., Dörner, S., Gratsea, M., Hendrick, F., Karagkiozidis, D., Lange, K., PETERS, A. J. M., Remmers, J., Richter, A., Van Roozendaal, M., Wagner, T., Wenig, M., and Loyola, D. G.: An improved TROPOMI tropospheric NO₂ research product over Europe, *Atmospheric Measurement Techniques*, 14, 7297–7327, <https://doi.org/10.5194/amt-14-7297-2021>, 2021.
- 535 Loyola, D.: Methodologies for solving Satellite Remote Sensing Problems using Neuro Computing Techniques, Ph.D. thesis, Technische Universität München, verlag Dr. Hut, ISBN 978-3-8439-1068-2, 2013.
- Loyola, D., Lutz, R., Argyrouli, A., and Spurr, R.: S5P/TROPOMI Algorithm Theoretical Basis Document Cloud Products, S5P-DLR-L2-ATBD-400I, issue 2.6.1, 2023.
- 540 Loyola, D. G.: Automatic cloud analysis from polar-orbiting satellites using neural network and data fusion techniques, in: IGARSS 2004. 2004 IEEE International Geoscience and Remote Sensing Symposium, vol. 4, pp. 2530–2533 vol.4, <https://doi.org/10.1109/IGARSS.2004.1369811>, 2004.
- Loyola, D. G., Thomas, W., Spurr, R., and Mayer, B.: Global patterns in daytime cloud properties derived from GOME backscatter UV-VIS measurements, *International Journal of Remote Sensing*, 31, 4295–4318, <https://doi.org/10.1080/01431160903246741>, 2010.
- 545 Loyola, D. G., Pedernana, M., and Gimeno García, S.: Smart sampling and incremental function learning for very large high dimensional data, *Neural Networks*, 78, 75–87, <https://doi.org/https://doi.org/10.1016/j.neunet.2015.09.001>, special Issue on "Neural Network Learning in Big Data", 2016.
- Loyola, D. G., Gimeno García, S., Lutz, R., Argyrouli, A., Romahn, F., Spurr, R. J. D., Pedernana, M., Doicu, A., Molina García, V., and Schüssler, O.: The operational cloud retrieval algorithms from TROPOMI on board Sentinel-5 Precursor, *Atmospheric Measurement Techniques*, 11, 409–427, <https://doi.org/10.5194/amt-11-409-2018>, 2018.
- 550 Lutz, R., Loyola, D. G., Gimeno García, S., and Romahn, F.: OCRA radiometric cloud fractions for GOME-2 on MetOp-A/B, *Atmospheric Measurement Techniques*, 9, 2357–2379, <https://doi.org/10.5194/amt-9-2357-2016>, 2016.
- Molina García, V.: Retrieval of cloud properties from EPIC/DSCOVER, Ph.D. thesis, Technische Universität München, <https://mediatum.ub.tum.de/?id=1662361>, 2022.
- 555 Nakajima, T. and King, M. D.: Determination of the optical thickness and effective particle radius of clouds from reflected solar radiation measurements. I - Theory, *Journal of Atmospheric Sciences*, 47, 1878–1893, [https://doi.org/10.1175/1520-0469\(1990\)047<1878:DOTOTA>2.0.CO;2](https://doi.org/10.1175/1520-0469(1990)047<1878:DOTOTA>2.0.CO;2), 1990a.

- Nakajima, T. and King, M. D.: Asymptotic theory for optically thick layers: application to the discrete ordinates method, *Appl Optics*, 31, 7669–7683, <https://doi.org/10.1364/AO.31.007669>, 1990b.
- 560 NASA/LARC/SD/ASDC: CALIPSO Lidar Level 2 5 km Cloud Layer, V4-20, 10.5067/CALIOP/CALIPSO/LID_L2_05KMCLAY-STANDARD-V4-20, 2018.
- Rodgers, C. D.: Inverse Methods for Atmospheric Sounding: Theory and Practice, vol. 2 of *Atmospheric, Oceanic and Planetary Physics*, World Scientific, <https://doi.org/10.1142/3171>, 2000.
- Schuessler, O., Loyola, D. G., Doicu, A., and Spurr, R. J. D.: Information Content in the Oxygen A-Band for the Retrieval of Macrophysical
565 Cloud Parameters, *IEEE Transactions on Geoscience and Remote Sensing*, 52, 3246–3255, <https://doi.org/10.1109/TGRS.2013.2271986>, 2014.
- Siddans, R.: S5P-NPP Cloud Processor ATBD, Tech. Rep. S5P-NPPC-RAL-ATBD-0001, issue 1.0, <https://sentinel.esa.int/documents/247904/2476257/Sentinel-5P-NPP-ATBD-NPP-Clouds>, 2016.
- Siddans, R.: S5P-NPP Cloud Processor Algorithm Theoretical Basis Document, S5P-NPPC-RAL-ATBD-0001, issue 2.0.0, 2022.
- 570 Sneep, M.: S5P-KNMI-L2-0129-TN - Sentinel 5 precursor interband 2015 - 4.0.0., https://sentiwiki.copernicus.eu/_attachments/1673595/S5P-KNMI-L2-0129-TN%20-%20Sentinel%205%20precursor%20interband%202015%20-%204.0.0.pdf, 2015.
- Spurr, R. J. D.: VLIDORT: A linearized pseudo-spherical vector discrete ordinate radiative transfer code for forward model and retrieval studies in multilayer multiple scattering media, *J. Quant. Spectrosc. Ra.*, 102, 316–342, <https://doi.org/10.1016/j.jqsrt.2006.05.005>, 2006.
- Spurr, R. J. D., Loyola, D., Heue, K.-P., Van Roozendaal, M., and Lerot, C.: S5P/TROPOMI Total Ozone ATBD, Tech. Rep. S5P-L2-DLR-
575 ATBD-400A, issue 2.3, Deutsches Zentrum für Luft- und Raumfahrt e.V. in der Helmholtz Gemeinschaft and Royal Belgian Institute for Space Astronomy (BIRA-IASB), <https://sentinel.esa.int/documents/247904/2476257/Sentinel-5P-TROPOMI-ATBD-Total-Ozone>, 2021.
- Theys, N., De Smedt, I., Yu, H., Danckaert, T., van Gent, J., Hörmann, C., Wagner, T., Hedelt, P., Bauer, H., Romahn, F., Pedergnana, M., Loyola, D., and Van Roozendaal, M.: Sulfur dioxide retrievals from TROPOMI onboard Sentinel-5 Precursor: algorithm theoretical basis, *Atmospheric Measurement Techniques*, 10, 119–153, <https://doi.org/10.5194/amt-10-119-2017>, 2017.
- 580 Van de Hulst, H. C.: *Light scattering by small particles*, Wiley, NY, 1957.
- Veefkind, J., Aben, I., McMullan, K., Förster, H., de Vries, J., Otter, G., Claas, J., Eskes, H., de Haan, J., Kleipool, Q., van Weele, M., Hasekamp, O., Hoogeveen, R., Landgraf, J., Snel, R., Tol, P., Ingmann, P., Voors, R., Kruizinga, B., Vink, R., Visser, H., and Levelt, P.: TROPOMI on the ESA Sentinel-5 Precursor: A GMES mission for global observations of the atmospheric composition for climate, air quality and ozone layer applications, *Remote Sensing of Environment*, 120, 70–83, <https://doi.org/10.1016/j.rse.2011.09.027>, the Sentinel
585 Missions - New Opportunities for Science, 2012.
- Walther, A. and Heidinger, A. K.: Implementation of the Daytime Cloud Optical and Microphysical Properties Algorithm (DCOMP) in PATMOS-x, *Journal of Applied Meteorology and Climatology*, 51, 1371–1390, <https://doi.org/10.1175/JAMC-D-11-0108.1>, 2012.
- Walther, A. and Straka, W.: Algorithm Theoretical Basis Document For Daytime Cloud Optical and Microphysical Properties (DCOMP), Version 1.2, https://www.star.nesdis.noaa.gov/jpss/documents/ATBD/ATBD_EPS_Cloud_DCOMP_v1.2.pdf, 2020.
- 590 Winker, D., Pelon, J., and McCormick, M.: The CALIPSO mission: Spaceborne lidar for observation of aerosols and clouds, *Proc. SPIE-Int. Soc. Opt. Eng.*, 4893, 1–11, <https://doi.org/10.1117/12.466539>, 2003.
- Winker, D., Hunt, W., and Hostetler, C.: Status and performance of the CALIOP lidar, *Proceedings of SPIE - The International Society for Optical Engineering*, 5575, <https://doi.org/10.1117/12.571955>, 2004.
- Winker, D. M., Hunt, W. H., and McGill, M. J.: Initial performance assessment of CALIOP, *Geophysical Research Letters*, 34,
595 <https://doi.org/10.1029/2007GL030135>, 2007.